NASA/CR-1998-206947

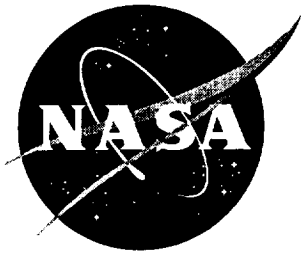

Euler Technology Assessment for Preliminary Aircraft Design - Unstructured/Structured Grid NASTD Application for Aerodynamic Analysis of an Advanced Fighter/Tailless Configuration

Todd R. Michal
Boeing Company, St. Louis, Missouri

National Aeronautics and
Space Administration

Langley Research Center
Hampton, Virginia 23681-2199

Prepared for Langley Research Center
under Contract NAS1-20342

March 1998

Available from the following:

NASA Center for AeroSpace Information (CASI)
800 Elkridge Landing Road
Linthicum Heights, MD 21090-2934
(301) 621-0390

National Technical Information Service (NTIS)
5285 Port Royal Road
Springfield, VA 22161-2171
(703) 487-4650

TABLE OF CONTENTS

SUMMARY

This study supports a NASA project aimed at determining the viability of using Euler technology for preliminary design use. The primary objective of this study was to assess the accuracy and efficiency of the Boeing, St. Louis unstructured grid flow field analysis system, consisting of the MACGS grid generation and NASTD flow solver codes. Euler solutions about the Aero Configuration/Weapons Fighter Technology (ACWFT) 1204 aircraft configuration were generated. Several variations of the geometry were investigated including a standard wing, cambered wing, deflected elevons, and deflected body flap. A wide range of flow conditions, most of which were in the non-linear regimes of the flight envelope, including variations in speed (high subsonic/transonic, supersonic), angles of attack, and sideslip were investigated. Several flowfield non-linearities were present in these solutions including shock waves, vortical flows and the resulting interactions. The accuracy of this method was evaluated by comparing solutions with test data and Navier-Stokes solutions. The ability to accurately predict lateral-directional characteristics and control effectiveness was investigated by computing solutions with sideslip, and with deflected control surfaces. Problem set up times and computational resource requirements were documented and used to evaluate the efficiency of this approach for use in the fast paced preliminary design environment.

The use of unstructured grids was found to significantly decrease the cycle time of NASTD applications primarily through a reduction in grid generation time. The efficiency and robustness of this method, while still too slow for generating an entire aerodynamic database, are sufficient to provide data at a large number of points across the flight envelope. The accuracy was generally sufficient for preliminary design use up to moderate angles of attack (~15 degrees). The prediction of aerodynamic effects due to control surface deflections were of mixed accuracy. Aerodynamic predictions of the elevon control effectiveness and the lateral-directional characteristics due to asymmetric control deflections were accurately predicted while the control effectiveness in pitch was consistently over-predicted. Less accurate aerodynamic predictions were obtained for control devices that generate a large amount of wake like separation such as the body flap.

Euler technology has strong relevance to preliminary-design applications. This technology provides a means of predicting non-linear aerodynamic effects that previously could only be obtained in the wind tunnel. This study has indicated that an un-exploited potential exists for development of a lateral-directional design tool. However, further work is needed to determine the parts of the flight envelope where this technology should or should not be used. Additional work may also be required to develop empirical calibration for some applications. The greatest benefit of this technology will be realized when it is tied to advances in multi-disciplinary design tool development.

INTRODUCTION

Over the past decade, great strides have been made in the development of preliminary design tools in the airplane radar signature and structural analysis disciplines. In contrast, aerodynamic analysis in preliminary design continues to rely primarily on linear tools developed several decades ago. The limitations of these methods are becoming increasingly apparent with the advent of low observable and unmanned aircraft technology.

These technologies have led to non-traditional vehicle shapes and control surface devices that exhibit highly non-linear aerodynamic behavior. Aerodynamic tools based on linear aerodynamic methods are inadequate for these types of aircraft, particularly at the edges of the flight envelope such as high angles of attack. For such applications, wind tunnel testing and/or non-linear analysis is required.

Until recently, Computational Fluid Dynamics (CFD) Euler or Navier-Stokes methods have been used very little in the preliminary design environment. This is primarily due to long cycle times and unvalidated accuracy levels. Computational hardware improvements and CFD technological developments, such as the advent of unstructured grids, have greatly reduced cycle times making Euler CFD methods a viable candidate for preliminary design use. Incorporation of these methods into the preliminary design process enables analytical determination of non-linear aerodynamic properties that currently can only be assessed in the wind tunnel. These methods could therefore potentially reduce the amount of costly wind tunnel testing. Another benefit of using CFD in preliminary design is the potential for the development of a multi-disciplinary design tool. Such a tool would allow the aerodynamic design to be tightly integrated with the design of other disciplines.

Despite these potential advantages, CFD methods have not found their way into the preliminary design environment. One reason for this may be the uncertainty associated with using a new technology. There are several risks involved in using Euler CFD methods for preliminary design. Errors are introduced into the analytical predictions by neglecting the effects of viscosity. The significance of this error varies with the problem geometry and flow conditions. The ability to account for this error is well documented for many problems such as attached flows at low to moderate angles of attack, however, for some cases the consequences of neglecting viscosity are difficult to predict. In addition, the ability of Euler CFD methods to predict lateral-directional characteristics and the effects from non-traditional control devices are not proven. It is also unclear whether the improvements that have been made in CFD cycle time are sufficient to meet the needs of the fast paced preliminary design environment.

A few years ago, NASA Langley Research Center initiated a project (Ref. 1-6) to evaluate the viability of a series of Euler CFD methods for use in preliminary design. This report summarizes the assessment of the Boeing, St. Louis developed CFD tools, MACGS and NASTD, for use in preliminary design. These tools provide for rapid analysis of complex configurations using either structured or unstructured grid techniques. This study was focused on the assessment of the unstructured grid Euler capability of these tools. NASTD/MACGS applications are performed within an integrated process whereby the grids are generated directly on the CAD model. A common database file is carried throughout the process from grid generation through post processing. To avoid the requirement for a mainframe- or super-computer, which often is not available in the preliminary design environment, solutions are computed in parallel on a network of workstations. This provides rapid turnaround and low memory usage. These tools have been used extensively on Boeing, St. Louis production programs such as the F/A-18 E/F, F-15C and AV-8B.

There were four primary objectives in this study. These were to assess the effects of viscosity over a range of Mach number and angle of attack, assess aerodynamic

predictions for non-traditional control devices, evaluate lateral-directional analysis capabilities, and document convergence-performance characteristics.

APPROACH

MACGS and NASTD were applied to the analysis of the Aero Configuration/Weapons Fighter Technology (ACWFT) 1204 configuration shown in Figure 1. This configuration was tested extensively (Ref. 7) in the NASA Langley Research Center 8 ft. Transonic Pressure Tunnel. The ACWFT configuration is representative of advanced preliminary designs. It is a tailless aircraft with a chined forebody. Two wing geometries were tested with the ACWFT model. The baseline wing has +/-30 degree leading and trailing edge sweeps, an aspect ratio of 2.65, and a taper ratio 0.132. The baseline wing cross section consists of a modified NACA 65A004 airfoil with a sharp leading edge. The alternate wing model consisted of the same planform as the baseline wing with the addition of camber and twist. The test model contained several non-traditional control devices including elevons, and body flaps. A flow through duct connecting the inlet and nozzle was incorporated into the test model. Test results included force and moment measurements and pressure tap data over the wing surface. In addition, pressure sensitive paint was used to obtain the global surface pressure distribution over the aircraft.

For this study, CFD solutions were computed on the ACWFT vehicle in six different configurations as shown in Figure 2. These configurations included the baseline configuration, baseline fuselage with a cambered/twisted wing, baseline configuration with afterbody flap deflected 90 degrees, baseline configuration with symmetric elevon deflections of -20 degrees, baseline configuration with asymmetric elevon deflections of +/- 20 degrees, and the baseline configuration with sideslip. The baseline, cambered wing, and symmetric elevon configurations were modeled assuming symmetry about the fuselage centerline. While developing the CFD model of the cambered wing configuration, we were unable to locate the geometric definition of the cambered wing/ fuselage interface that was used on the wind tunnel test model. For this study an interface was made up by blending the cambered wing geometry into the baseline wing root section. Unfortunately, the results presented below show that this geometry modification may have influenced the resulting CFD drag predictions.

A summary of the CFD run matrix is shown in Figure 3. For each configuration, Euler solutions were computed at flow conditions of Mach 0.6, angles of attack of 10, 15, and 20 degrees, Mach 0.9 at angles of attack of 10 and 15 degrees, and Mach 1.2 at 10 degrees angle of attack. In addition to the Euler solutions, Navier-Stokes CFD solutions were computed about the baseline and cambered/twisted wing configurations at the same flow conditions to isolate the aerodynamic effects due to viscosity.

Grid Generation

Grid generation was performed using MACGS (Refs. 8,9), which is a general purpose, arbitrary topology grid generation system developed at the McDonnell Douglas Corporation. It supports the generation of multi-zone structured and/or unstructured grids. MACGS is comprised of three modules: ZONI3G, GMAN, and GPRO. ZONI3G is used to generate structured and/or unstructured surface grids. GMAN provides the capability to

generate volume grids, specify boundary conditions and generate coupling information between structured and/or unstructured grid zones. GPRO manipulates zones (such as transforming, splitting, and combining) and supports inputting and outputting files in various formats. The interactive, graphical user interfaces of ZONI3G and GMAN support both the novice and expert user.

A dual grid approach was used in this study where all viscous computations were performed on a pre-existing structured grid and all Euler solutions were computed on unstructured grids. Unstructured grid generation was performed using the four step process shown in Figure 4. In the design environment, the geometry residing in the CAD system often contains detailed geometry components or surface gaps that the CFD user does not want to include in the analysis. The first step in the grid generation process is to modify the surface geometry to remove these unwanted geometry components and fill any remaining gaps or holes. An unstructured surface grid is then interactively generated on the clean surface representation. Grid resolution is controlled by the user through specification of boundary edge distributions for each surface patch and through several line and point source options. A tetrahedral volume grid is then generated within MACGS using a Delauney point insertion approach. Grid swapping and smoothing are used to ensure the quality of the final grid. Resolution of the volume grid is set by the surface grid spacing and by two user specified parameters that control the global cell spacing and the amount of clustering near the geometric surface. The resulting grid is partitioned into multiple blocks with the METIS algorithm (Ref. 10). The sizes of each block are selected to balance the solution load on parallel computational systems.

The structured and unstructured surface grids for the baseline ACWFT configuration are shown in Figure 5. The multi-zone structured grid was generated in MACGS during a previous study funded by Wright Laboratory (Ref . 7). The inlet and nozzle ducts were treated differently in the unstructured and structured grids. To simplify grid generation, the inlet and nozzle ducts were faired over in the structured grid. For all but two of the unstructured grids, the inlet duct was modeled up to the compressor face (where a mass flow boundary condition was specified) and the nozzle duct was faired over. For the symmetric and asymmetric deflected elevon unstructured grids, a flow through duct was modeled that connected the inlet and nozzle faces. This was done to capture the effects of the nozzle flow washing over the deflected elevon surfaces.

The sizes of the resulting unstructured surface grids are shown in Figure 6. The surface grids ranged in size from 150,000 to 300,000 triangles. Cuts through the structured and unstructured volume grids are shown in Figure 7. In the first of the cuts shown in the top of Figure 7, the lower surface of the structured grid differs from the unstructured surface due to the inlet duct fairing. In Figure 8, the surfaces of the unstructured baseline grid are shown after grid partitioning. In this example, the unstructured grid has been partitioned into ten equal size zones.

The sizes of the structured and unstructured grids are summarized in Figure 9. The sizes of the unstructured grids ranged from just over 1 million cells for the baseline configuration to 2.7 million cells for the asymmetrically deflected elevon grid. The viscous structured grids contained about 2.7 million nodes. Labor hours for the unstructured grid generation are shown in Figure 10. The baseline unstructured grid required 30 person hours to generate. Grid generation for the other five configurations examined in this study

were made by making minor modifications to the baseline surface grid. These modifications required only a few person hours for each configuration. The computational time required to generate each unstructured grid is shown in Figure 11. The CPU times given are for a Silicon Graphics R10,000 processor and range from 1.5 hours to almost 3 hours.

Flow Solution Methodology and Performance Characteristics

The solution computations in this study were performed using the NASTD flow solver. This flow solver was developed by the McDonnell Douglas Corporation, and can run on structured, unstructured or a combination of structured and unstructured grids. It supports multi-block and overlapping (chimera) grids. It runs in serial or parallel on a wide variety of machines. A complete description of the NASTD structured grid solution algorithm is given in Reference 11. The structured grid algorithm solves any subset of the full Reynolds averaged Navier-Stokes equations. Options include Euler, thin layer, parabolized Navier-Stokes and full Navier-Stokes calculations. Turbulence can be modeled by a variety of algebraic, one- and two-equation turbulence models. The solution algorithm can be selected zonally by the user. The default time integration scheme is a first-order, approximately factored implicit scheme. For inviscid flows (or, under the thin layer approximation, for directions without viscous terms) the implicit operator is diagonalized, providing a significant speed-up. Explicit Runge Kutta options of up to third-order are also available for time accurate flowfields. For steady-state flows, variable time steps based on local eigenvalues are used to speed convergence. Grid sequencing is available to speed convergence on large grids. The default explicit spatial operator is a second-order flux difference splitting scheme, also known as Roe's scheme. The standard upwind operator has been replaced by a mixed scheme which retains the upwind scheme stability properties with reduced numerical dissipation. Optionally, the scheme may be switched to various first- through fifth-order schemes and total variation diminishing (TVD) limiters may be activated. Other available schemes include standard second-order central differencing with added second- and fourth-order dissipation.

A complete description of the NASTD unstructured grid algorithm and the parallel implementation is given in References 12 and 13. This algorithm is a node-based upwind finite-volume unstructured grid algorithm. The implementation used for this study solves the Euler equations on tetrahedral cell grids. Higher-order computations are achieved using a least squares reconstruction scheme with flux limiting. The numerical flux values are computed at the mid-point of each edge using Roe's approximate Riemann solver. Flowfield variables are stored at grid nodes and flux computations are performed at each grid edge. This results in relatively low storage requirements and run times. Time integration is performed using an explicit point Jacobi or Runge-Kutta algorithm for each node.

The following NASTD options were used in the computations for this study. The fluxes were computed using a second-order accurate Roe's scheme with a Total Variational Dimensioning (TVD) limiter in the case of the structured solutions and a monotone limiter for the unstructured cases. In the structured grid Navier-Stokes computations, turbulence was modeled with the Spalart-Almaras turbulence model. An implicit approximate factorization algorithm was used for the time integration of the structured grid cases and an

explicit Runge-Kutta scheme was used for the unstructured grid cases. Solution convergence was determined by monitoring the integrated lift, drag and pitching moments. For the viscous cases the friction drag was also monitored. No attempt was made to find the maximum CFL number for these cases. Instead a "safe" CFL number was selected based on past experience. CFL numbers ranged from 0.3 to 0.7 for the unstructured computations and 1.0 to 3.0 for the structured grid computations.

Two representative examples of Euler solution convergence from this study are shown in Figures 12 and 13. These examples represent the best (Figure 12), and worst (Figure 13) Euler solution convergence histories from this study. In these figures, the lift coefficient is plotted versus the solution cycle number. In Figure 12 the convergence for the baseline configuration at Mach 1.2, 10 degrees angle of attack and 5 degrees sideslip is shown. This solution was restarted from the 0 degree sideslip solution at 700 cycles. The lift coefficient reaches a steady value after an additional 1800 cycles (for a total of 2500 cycles). In Figure 13 the lift coefficient versus cycle number is shown for the baseline configuration with -20 degree symmetric elevon deflections at Mach 0.6 and 20 degrees angle of attack. This solution was run with the first-order accurate scheme for 1800 cycles and then switched to the second-order scheme. The lift coefficient did not converge to a steady value but instead oscillated about an average. This behavior was observed in all of the 20 degree angle of attack cases and is most likely due to a non-steady behavior in the flow field.

The convergence properties of the NASTD Navier-Stokes solutions about the baseline configuration at Mach 0.6, 10 and 20 degrees angle of attack are shown in Figures 14 and 15. These solutions were run for 680 cycles on a sequenced grid (every other grid point removed in all three directions). The solution was then switched to the full grid and reached convergence after another 500 cycles. The Navier-Stokes solutions did not experience the oscillatory behavior at the high angles of attack seen in the Euler solutions. This could be due to the viscous terms which add additional diffusion to the flow.

Run times for the Euler solutions are summarized in Figure 16. The minimum, average, and maximum run time are shown for each configuration. The numbers shown represent the total CPU time and were obtained by multiplying the CPU time/iteration/cell by the number of cells and the number of iterations. The times do not include the savings obtained by running on a parallel computational system. For instance the average baseline configuration solution required 90 hours of CPU time. When this solution was run on a cluster of ten workstations, the actual clock time was a little under 10 hours. The memory requirements for each of the Euler solutions are summarized in Figure 17. These memory requirements are presented as though the solution were run as a single zone on one processor. The actual memory requirements per machine varied depending on the number of grid partitions. For ten equal size partitions, the memory requirements are 1/10 the total. Solution run times and memory requirements for the Navier-Stokes solutions are summarized in Figures 18a and b. Once again these numbers are given for a single zone solution on a single processor. The actual requirements were much lower when running in parallel.

RESULTS

Baseline Configuration

Euler and Navier-Stokes solutions were generated on the baseline ACWFT configuration. Comparisons of the Euler and Navier-Stokes solutions were made to identify the error introduced in the Euler solutions by neglecting viscosity. Further comparisons with test data were made to identify the accuracy of the CFD methods. In addition, differences between the baseline and other configuration results were used to measure the incremental effects of each configuration.

Contours of the predicted surface pressure coefficient and traces of the streamlines for the Euler and Navier-Stokes results at Mach 0.6, and angles of attack of 10, 15 and 20 degrees are shown in Figure 19. In this Figure, the Euler solution is shown on the left half of the aircraft and the corresponding Navier-Stokes solution is shown on the right half of the aircraft. At 10 degrees angle of attack, the Euler and Navier-Stokes results are very similar. Both solutions predict a vortex separating off of the chined forebody and another off of the wing leading edge. At 15 degrees angle of attack the surface pressures are once again very similar. Both solutions indicate vortices similar to the 10 degree angle of attack case. At 20 degrees angle of attack the differences between the Euler and Navier-Stokes solutions are more noticeable both in terms of surface pressure distribution and particle traces. In the Euler solution the wing leading edge vortex appears to have burst. This results in significant differences in the surface pressures between the Euler and Navier-Stokes solutions on the upper surface of the wing.

Total pressure contours at fuselage stations of 260 in., 420 in. and 510 in. are shown in Figures 20 and 21. The locations and strengths of the predicted vortices for the Euler and Navier-Stokes solutions are very similar at 10 degrees angle of attack. At 20 degrees angle of attack, however, the Navier-Stokes solution indicates a larger total pressure loss in the vortex cores and the structure of the vortices are considerably different.

The effect of viscosity on the predicted solutions at different Mach numbers is presented in Figure 22. In this figure, surface pressure coefficient contours and streamline traces from the Euler and Navier-Stokes solutions at 10 degrees angle of attack and Mach numbers of 0.6, 0.9, and 1.2 are compared. The streamline patterns predicted by the Euler and Navier-Stokes solutions are similar at all three Mach numbers. However, there are several differences in the predicted surface pressures at Mach 0.9. As expected, the Euler solution indicates a strong shock over the wing at about 75% chord, while the Navier-Stokes solution predicts a more diffused footprint of the shockwave that is slightly further forward. This is probably due to shock boundary-layer interaction effects that the Euler solution is missing. At Mach 1.2, the shock has moved aft of the wing trailing edge and the Euler and Navier-Stokes solutions agree fairly well.

Pressure coefficient contours on the lower surface for the Euler and Navier-Stokes solutions are compared in Figure 23. The results agree well except near the inlet where the two solutions have a different treatment of the inlet geometry (faired over for Navier-Stokes and flow through for the Euler). While having little influence on the upper surface solution, the different inlet models significantly change the lower surface results.

A comparison of surface pressures from the CFD results and pressure sensitive paint (PSP) test data is shown in Figures 24 and 25 for flow conditions of Mach 0.6, and

Mach 0.9 at 15 degrees angle of attack. The PSP data was not calibrated to provide a quantitative value for each color. Instead, the color map used for plotting the CFD results was selected to attempt to match the colors of the PSP data thus providing a qualitative comparison of the flowfield structures such as shock waves. At Mach 0.6, the Euler, Navier-Stokes, and PSP contours are very similar. At Mach 0.9 the test data compares favorably with the Navier-Stokes results while, as expected, the Euler results clearly miss the shock boundary layer interaction on the wing.

In addition to the PSP pressure data, surface pressure taps were placed at four spanwise locations on the test model. Comparisons of the CFD surface pressures with measurements taken at the pressure taps are made in Figures 26 through 31. In Figures 26 through 28, results from the solutions at Mach 0.6, angles of attack of 10, 15 and 20 degrees are shown. At angles of attack of 10 and 15 degrees, the Euler and Navier-Stokes results are similar with the exception of the suction peak at the leading edge. As expected, the Euler solution over predicts the acceleration around the sharp wing leading edge. At 20 degrees angle of attack there are significant differences in the Euler and Navier-Stokes surface pressures. This is consistent with the differences that were observed in the surface pressure contour plots above. Comparisons of the CFD results with the pressure tap data at Mach 0.9 are shown in Figures 29 and 30. As expected, the Euler solutions predict a shock location that is slightly aft of that predicted by the Navier-Stokes solutions. In addition, there is a considerable amount of smearing of the shock footprint evident in the Navier-Stokes results and test data that, is not present in the Euler solution. In Figure 31 the CFD surface pressures are compared with pressure tap data at Mach 1.2 and 10 degrees angle of attack. At this flow condition, the shock has left the wing surface and the Euler and Navier-Stokes solutions compare favorably with the test data.

Force predictions were obtained from the CFD solutions by integrating the surface pressures (and skin friction for the Navier-Stokes solutions) over the aircraft surface. Corrections were added to the Euler drag estimates to account for the skin friction drag. The corrections were obtained using the following procedure. First, Euler solutions were computed over the baseline configuration at angles of attack that resulted in zero lift, and Mach numbers of 0.6, 0.9, and 1.2. Next, the zero lift drag predicted by each Euler solution was subtracted from the zero lift drag measured in the test at the same Mach number to obtain the skin friction contribution to the total drag. The resulting skin friction estimates were then added to all the Euler estimates. For the Euler solutions that failed to converge to a steady state, force and moment values were obtained by averaging the integrated results over the last few hundred cycles of the solution. Error bars are drawn to indicate the maximum and minimum oscillation about the average. The CFD force and moment predictions are compared with test data in Figures 32 through 34. The lift and drag from the Euler solutions match the test data very well with the exception of the Mach 0.9, 15 degrees angle of attack. This is probably due to the missing shock boundary layer interaction effects in the Euler solution. Surprisingly, the Navier-Stokes force and moment results are slightly worse than the Euler predictions. The most likely reason for this discrepancy is the presence of the faired over inlet model used in the viscous computations.

Cambered Wing Configuration

An alternate wing was tested on the ACWFT geometry. This wing was similar to the ACWFT baseline wing with the addition of camber and twist. Contours of the predicted surface pressure coefficient and streamline traces are compared for the Euler and Navier-Stokes cambered wing configuration solutions at Mach 0.9, 10 degrees angle of attack in Figure 35. The comparison is similar to the baseline wing comparisons showing that the Euler solution is missing the shock boundary layer interaction effects. The force and moment predictions are compared with the test data in Figures 36-38. Again these comparisons are very similar to the baseline wing results. The most notable deviations from the test data occur at flow conditions of Mach 0.6, 20 degrees angle of attack and Mach 0.9, 15 degrees angle of attack. Increments in the force and moment predictions between the cambered wing and baseline wing configurations are shown in Figures 39-41. The test data shows a slight increase in lift and decrease in drag with little change in pitching moment. The Euler and Navier-Stokes results also predict a slight increase in lift, however, both methods predict an increase in drag. This discrepancy from the test data may be partially attributed to an increase in interference drag caused by the method employed to attach the alternate wing in the CFD grid.

Lateral-Directional Characteristics

The ability to compute lateral-directional characteristics is essential for a preliminary design tool. The baseline configuration was run at 5 degrees sideslip to evaluate the lateral-directional characteristic prediction capability of the present Euler method. Streamline traces and surface pressure predictions from the Euler solutions at Mach 0.6, 15 degrees angle of attack with 0 and 5 degrees sideslip are compared in Figure 42. The sideslip has little effect on the surface pressures. The most notable effect of the sideslip is the change in track of the vortices downstream of the aircraft with little effect over the aircraft itself. Force and moment predictions are compared with test data in Figures 43-45. Increments in the force and moment predictions between the sideslip and zero sideslip cases are shown in Figures 46-48. The test data indicates large increments in the lift, drag and moments while the CFD results indicate small changes in the forces and moments. The test data trends are contrary to the expected behavior of a tailless aircraft. We suspect that the location of the support strut on the model may have influenced the test data.

Control Devices

One of the objectives of this program was to evaluate the ability of the CFD method to compute the effects of control surfaces. Solutions were computed about three control devices including a symmetrically deflected elevon, asymmetrically deflected elevon, and a body flap.

The ACWFT solid surface model and a closeup of the surface grid about the symmetrically deflected elevon is shown in Figure 49. The elevon was deflected up 20 degrees on the left and right sides of the aircraft. Euler solutions were run at all six flow conditions. A comparison of the surface pressure and streamline traces for the baseline (undeflected elevon) and symmetrically deflected elevon cases at Mach 0.6, 15 degrees angle of attack is shown in Figure 50. The elevon deflection primarily affects the solution

near the tail and has little effect on the solution over the wing. The predicted lift, drag and pitching moment from the CFD solutions is compared with test data in Figures 51-53. Once again the CFD lift and drag predictions agree with the test data, however, the CFD results over predict the effect of the elevon deflection on pitch up. This can be seen in the incremental force and moment plots shown in Figures 54-56. The CFD and test data both indicate a substantial reduction in lift with a slight decrease in drag. The CFD results overpredict the effect of the elevon deflection on pitching moment.

The ACWFT solid surface model and a closeup of the surface grid about the asymmetrically deflected elevon and deflected body flap are shown in Figure 57. Surface pressure and streamline traces from the CFD solutions at Mach 0.6, 15 degrees angle of attack, with the devices are compared with the baseline solution in Figure 58. The asymmetrically deflected elevon has little effect on the solution other than in the tail region, whereas the body flap has a larger influence on the surface pressure of the surrounding geometry.

Force and moment predictions for the asymmetrically deflected elevon CFD solutions are compared with test data in Figures 59-61. The comparisons are similar to the previous results showing good agreement for lift and drag except at Mach 0.9, 15 degrees angle of attack. Increments in the force and moment predictions with the baseline results are shown in Figures 62-64. As expected the pitching moment increment is very small at all three Mach numbers. At Mach 0.6, the CFD results indicate an increase in lift and drag as the angle of attack is increased whereas the test data a constant increment in lift and a decreasing increment in drag. These discrepancies may be due to the lack of convergence of the Euler method at the high angles of attack. The incremental pitch, yaw and roll are well predicted by the CFD method.

Force and moment predictions for the deflected body flap CFD solutions are compared with test data in Figures 65-67. Once again the force comparisons are good with the exception of the transonic cases at Mach 0.9. Increments in the force and moment predictions with the baseline results are shown in Figures 68-70. The incremental data indicates a slight decrease in lift and increase in drag (for angles of attack less than 15 degrees). The CFD results underpredict the lift decrease due to the flap particularly at the higher angles of attack. The CFD drag increments are also much higher than the test data increments at the higher angles of attack. The discrepancies may be due to lack of convergence or poor modeling of the large wake like separated region aft of the flap. This type of flowfield is largely dominated by viscous effects and is not well modeled with an Euler method. The incremental pitch, roll and yawing moments due to the flap are well predicted by the CFD results.

CONCLUSIONS

This study has provided an assessment of the viability of using the NASTD unstructured grid Euler technology in preliminary design. Euler solutions about the ACWFT 1204 configuration with several geometry variations including baseline wing, cambered wing, deflected elevons, and deflected body flap were generated. A wide range of flow conditions, most of which were in the non-linear regimes of the flight envelope, were evaluated including transonic and high angle of attack flowfields. Several non-linearities were present in these solutions including shock waves, vortical and separated

flows. Comparisons with test data and Navier-Stokes solutions were used to evaluate the accuracy of this Euler method and to identify viscous effects for selected configurations and conditions. Solutions with sideslip and deflected control surfaces were compared with test data to evaluate the ability to accurately predict lateral-directional characteristics and control effectiveness.

The unstructured grid approach facilitated rapid modeling of the ACWFT configuration and its variations. Geometry variations such as flap deflections were modeled in only a few hours. The methodology proved to be very robust generating solutions for various surface control devices and various flow conditions with very few problems. Run times were sufficiently fast for use in the preliminary design environment with overnight run times possible on parallel computational systems. These cycle times are sufficient to generate data at a large number of points across the flight envelope, however, they are still too slow to generate an entire aerodynamic database typically developed during the wind tunnel test.

The Euler results captured several non-linear aerodynamic characteristics of the test data at high angles of attack. Force and moment predictions were generally sufficient for preliminary design use up to moderate angles of attack (~ 15 degrees) across the examined Mach number range. Less accuracy was obtained at high angles of attack and for control devices that generated a large amount of separation such as the body flap. One surprising result of this study was that Navier-Stokes force and moment results were not appreciably better than the Euler predictions. This indicates there is little benefit in stepping up to the longer run times and complexities of a Navier-Stokes method for these types of predictions.

One case where Navier-Stokes predictions may have provided better results than the Euler solutions is for the deflected afterbody flap. This control device generates a large separated region aft of the flap that interacts with the fuselage surface to generate changes in the force and moment distributions. The Euler method did a good job of predicting the flap control effects on the roll, yaw, and pitching moments but significantly over predicted the effect on lift and drag. Better predictions were obtained for the elevon control device effectiveness. The lateral-directional characteristics due to asymmetric control deflections were accurately predicted while the control effectiveness in pitch was consistently over-predicted. With further work, empirical correlations to compensate for the pitch effectiveness could be developed.

Euler technology has strong relevance to preliminary-design applications. This technology provides a means of generating non-linear and lateral-directional aerodynamic data that previously could only be obtained in the wind tunnel. The ability to analytically generate lateral-directional data provides an un-exploited potential for the development of a lateral-directional design tool based on existing Euler technology.

It is likely that linear aerodynamic tools will continue to be used to develop a large portion of the aerodynamic database. Further study is necessary to determine the parts of the flight envelope where linear and non-linear methods are best applied. Comparisons between linear and non-linear results although not a part of this study, could help guide this determination. Further study is also necessary to develop empirical calibrations of Euler results for some applications. This was evident in the elevon effectiveness predictions obtained in this study.

One of the greatest potential benefits of Euler technology may be the ability to tie non-linear aerodynamic data into a multi-disciplinary design tool. The ability to share data with other disciplines and use a common geometry database is essential if this technology is to be used successfully in the preliminary design environment.

ACKNOWLEDGEMENTS

This effort was sponsored by NASA-Langley Research Center under Contract NAS1-20342. Farhad Ghaffari was the contract Technical Monitor and provided invaluable technical guidance over the course of this study. His assistance is gratefully acknowledged.

REFERENCES

1.) Finely, D.B.,"Euler Technology Assessment Program for Preliminary Aircraft Design Employing SPLITFLOW Code With Cartesian Unstructured Grid Method," NASA CR-4649, March 1995.

2.) Kinard, T.A., Harris, B.W., and Raj, P.," An Assessment of Viscous Effects in Computational Simulation of Benign and Burst Vortex Flows on Generic Fighter Wind-Tunnel Models Using TEAM Code," NASA CR-4650, March 1995.

3.) Treiber, D.A. and Muilenberg, D.A.," Euler Technology Assessment for Preliminary Aircraft Design Employing OVERFLOW Code With Multiblock Structured-Grid Method," NASA CR-4651, March 1995.

4.) Finely, D.B. and Karman, Jr., S.L.,"Euler Technology Assessment for Preliminary Aircraft Design - Compressibility Predictions by Employing the Cartesian Unstructured Grid SPLITFLOW Code," NASA CR-4710, March 1996.

5.) Kinard, T.A. and Raj, P.," Euler Technology Assessment for Preliminary Aircraft Design - Compressibility Predictions by Employing the Unstructured Grid USM3D Code," NASA CR-4711, March 1996.

6.) Kinard, T.A., Finley, D.B., and Karman, Jr., S.L.,"Prediction of Compressibility Effects Using Unstructured Euler Analysis on Vortex Dominated Flow Fields," AIAA Paper-No. 96-2499, June 17-29,1996.

7.) O'Neil, P.J., Krekeler, G.C., Billman, G.M., and Creaseman, F.C., "Aero Configuration/Weapons Fighter Technology (ACWFT) - Summary Technical Report," WL-TR-95-3002, December 1994.

8.) Gatzke, T.D., et. al., "MACGS: A Zonal Grid Generation System for Complex Aero-Propulsion Configurations," AIAA-91-2156, June 1991.

9.) LaBozzetta, W.F., Gatzke, T.D., Ellison, S., Finfrock, G.P., and Fisher, M.S., "MACGS - Towards the Complete Grid Generation System," AIAA 94-1923, 12th AIAA Applied Aerodynamics Conference, June 20-22, 1994.

10.) Karypis, G., and Kumar, V.,"METIS, Unstructured Graph Partitioning and Sparse Matrix Ordering System", Users Manual August, 1995.

11.) Romer, W.W., and Bush, R.H., "Boundary Condition Procedures for CFD Analysis of Propulsion Systems - The Multi-Zone Problem," AIAA-93-1971, June 1993.

12.) Michal, T., and Halt, D., "Development and Application of an Unstructured Grid Flow Solver for Complex Fighter Aircraft Configurations," AIAA 95-1785, June, 1995.

13.) Michal, T., and Johnson, J., "A Hybrid Structured/Unstructured Grid Multi-Block Flow Solver for Distributed Parallel Processing," AIAA 97-1895, June, 1997.

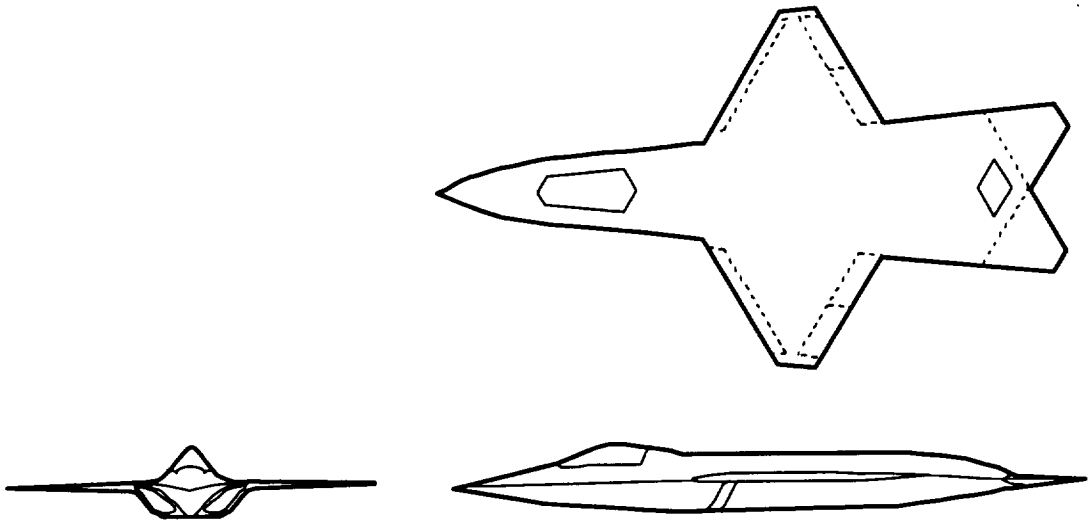

Figure 1. ACWFT 1204 Three View Drawing.

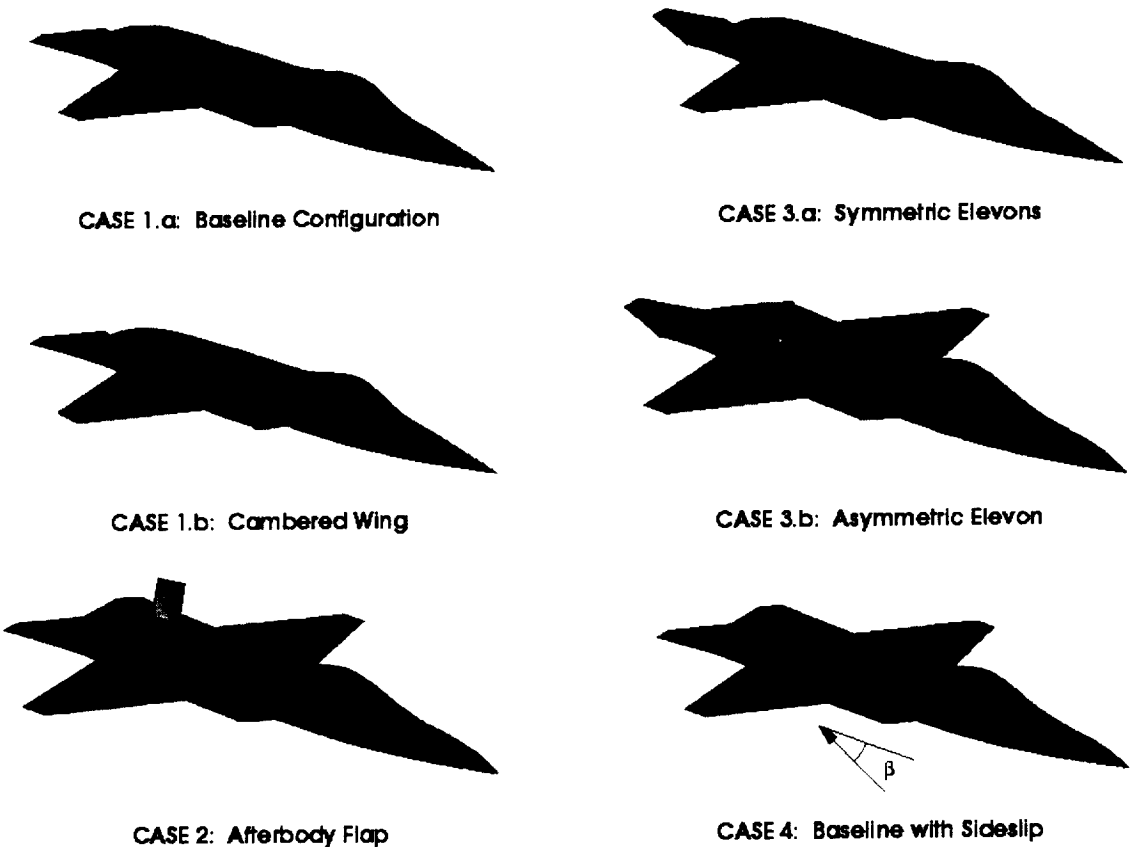

Figure 2. ACWFT 1204 Configurations Modeled in Euler Technology Assessment Study.

Case 1a: Baseline

α	Mach 0.6	Mach 0.9	Mach 1.2
10°	I,V	I,V	I,V
15°	I,V	I,V	
20°	I,V		

Case 1b: Cambered/Twisted Wing

α	Mach 0.6	Mach 0.9	Mach 1.2
10°	I,V	I,V	I,V
15°	I,V	I,V	
20°	I,V		

Case 2: After Body Flap

α	Mach 0.6	Mach 0.9	Mach 1.2
10°	I	I	I
15°	I	I	
20°	I		

Case 3a: Symmetric Elevons

α	Mach 0.6	Mach 0.9	Mach 1.2
10°	I	I	I
15°	I	I	
20°	I		

Case 3b: Asymmetric Elevons

α	Mach 0.6	Mach 0.9	Mach 1.2
10°	I	I	I
15°	I	I	
20°	I		

Case 4: Baseline with Sideslip

α	Mach 0.6	Mach 0.9	Mach 1.2
10°	I	I	I
15°	I	I	
20°	I		

I: Inviscid V: Viscous

Figure 3. Euler Technology Assessment CFD Run Matrix.

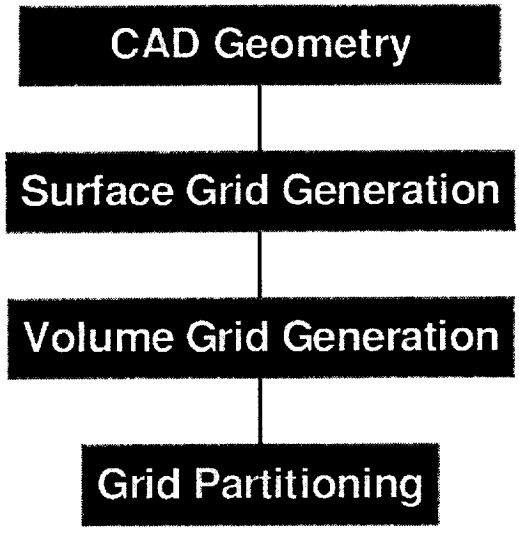

Figure 4. MACGS Unstructured Grid Generation Process.

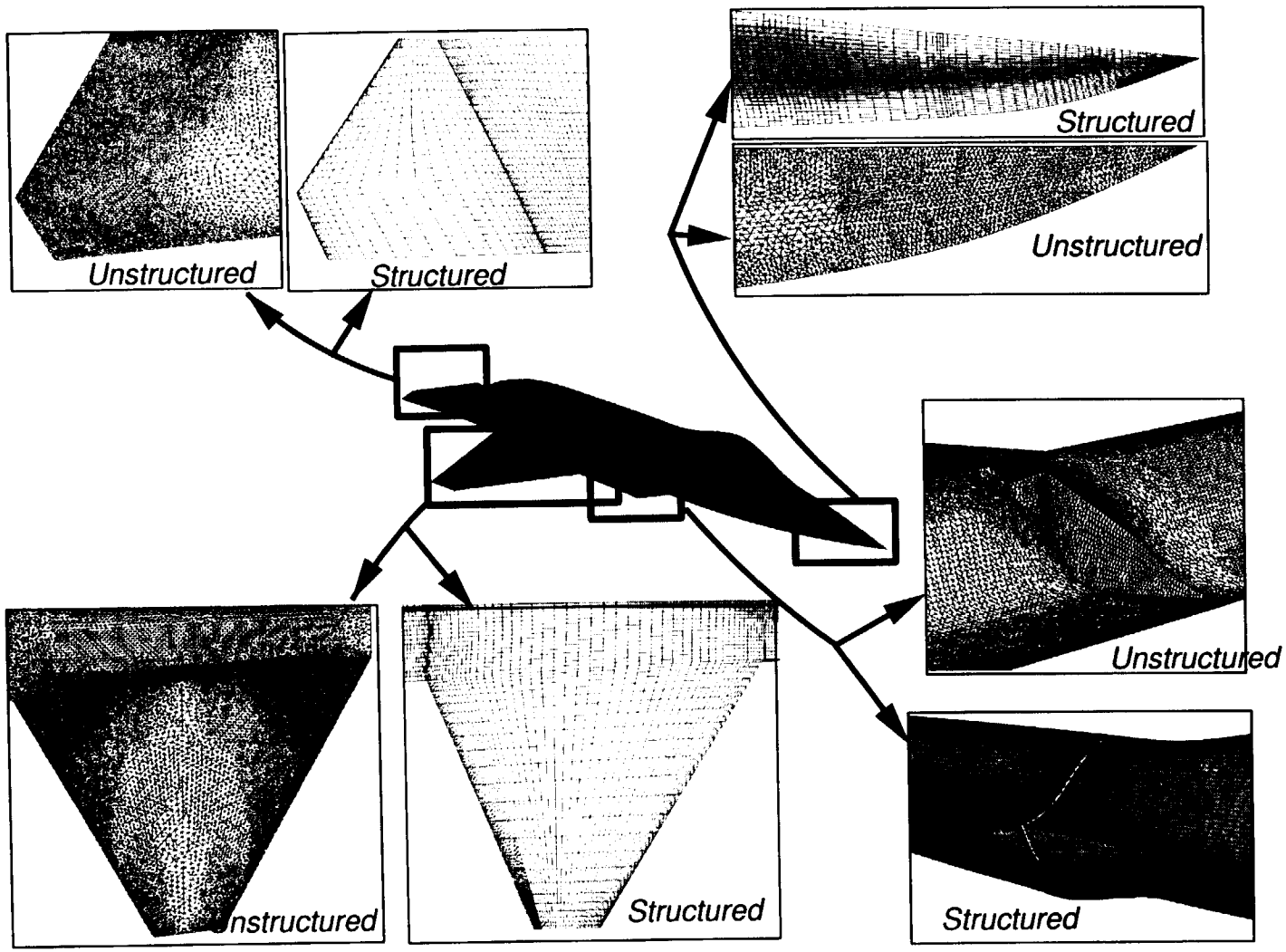

Figure 5. Surface Grids About the ACWFT 1204 Baseline Configuration.

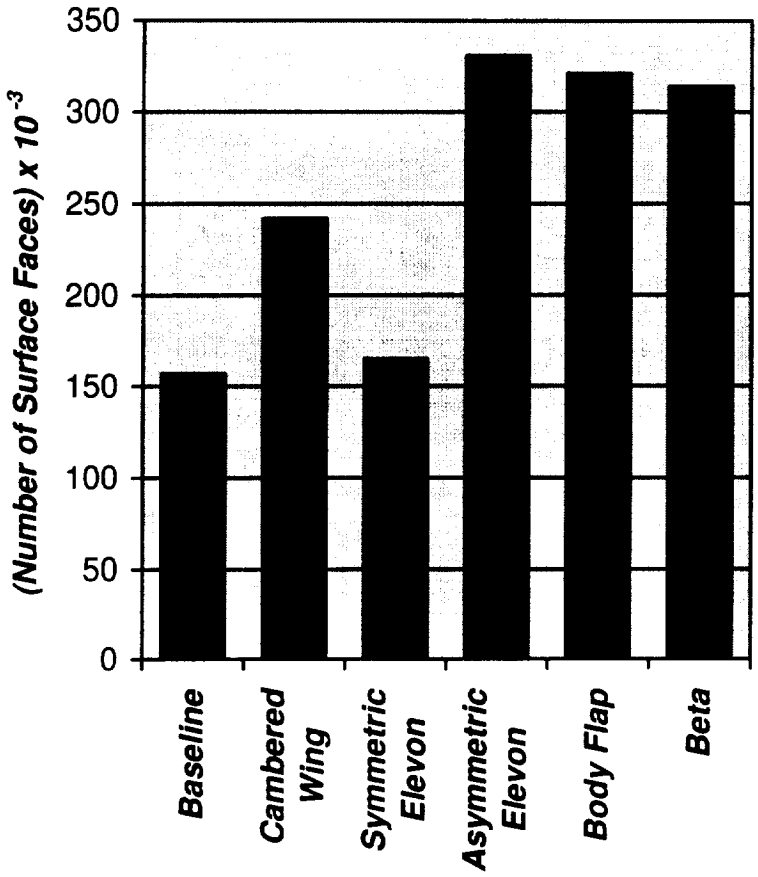

Figure 6. Unstructured Surface Grid Sizes, Six ACWFT 1204 Configurations.

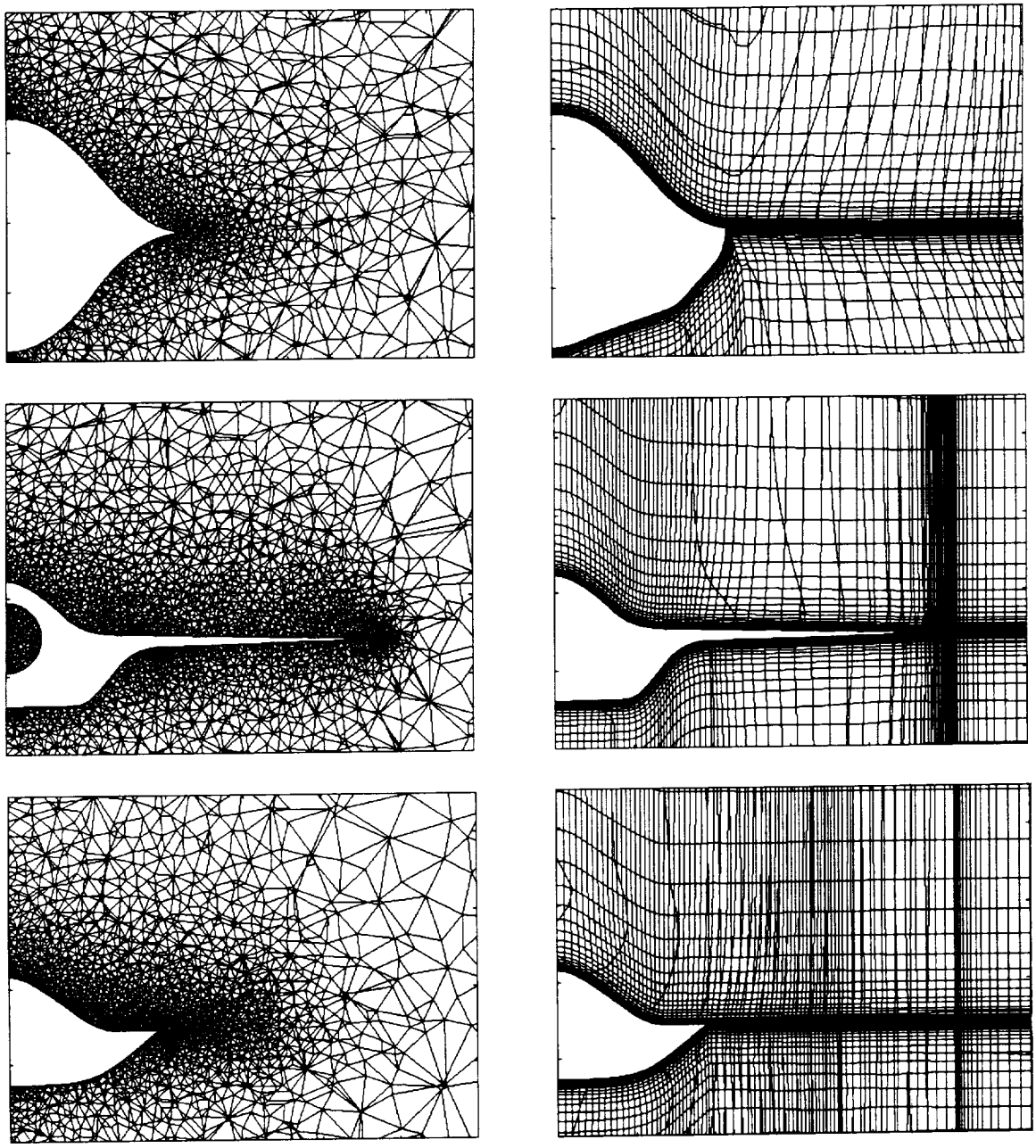

Figure 7. Cuts Through Volume Grids, ACWFT 1204 Baseline Configuration.

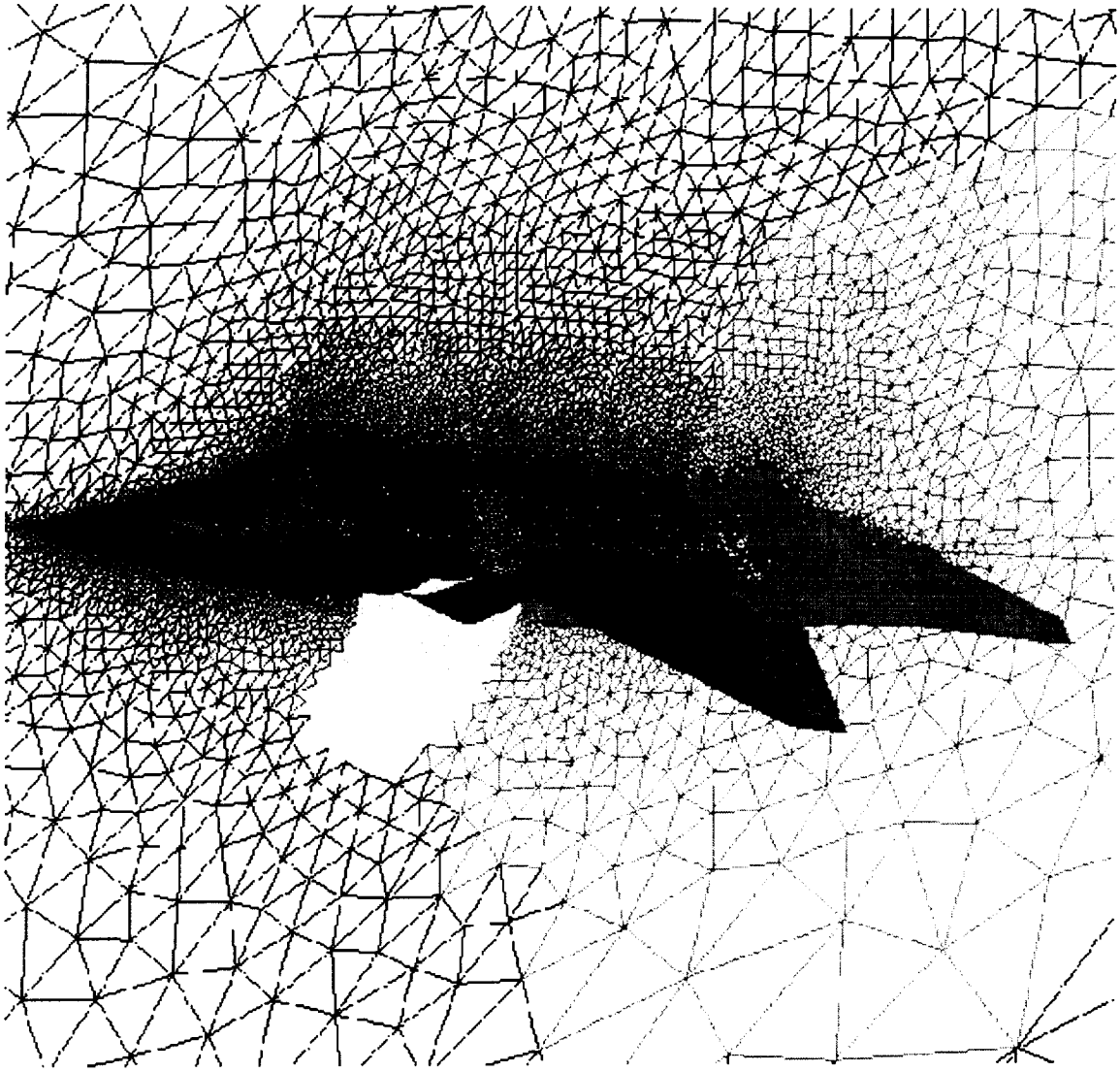

Figure 8. ACWFT 1204 Unstructured Surface Grid After Partitioning.

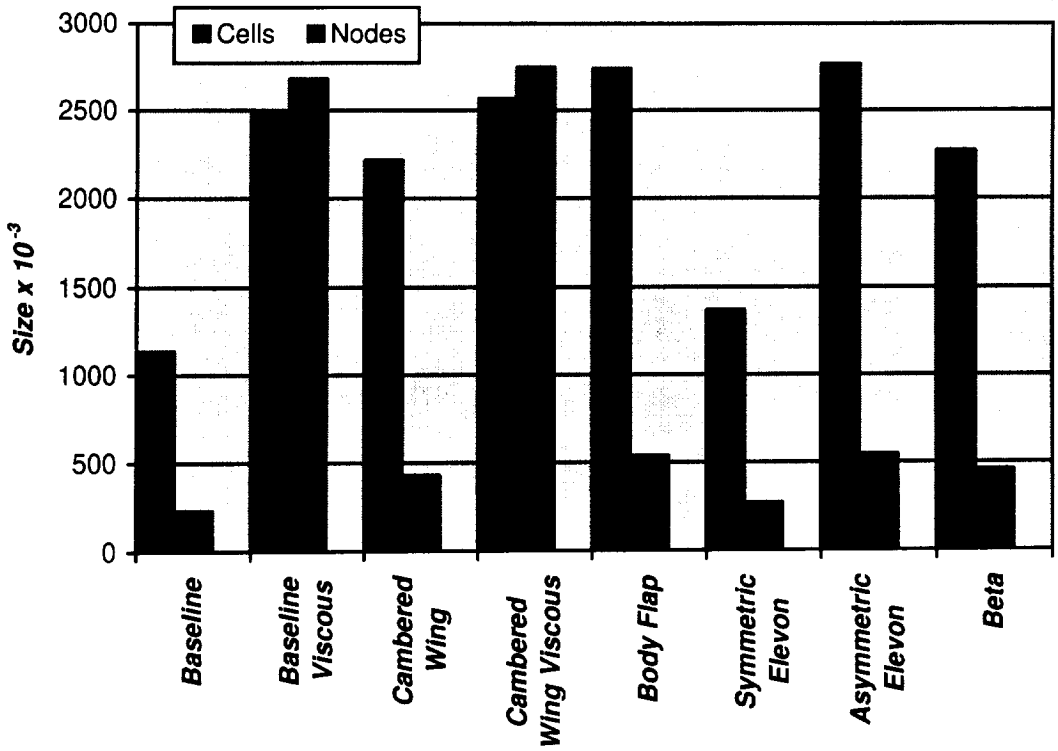

Figure 9. Volume Grid Sizes.

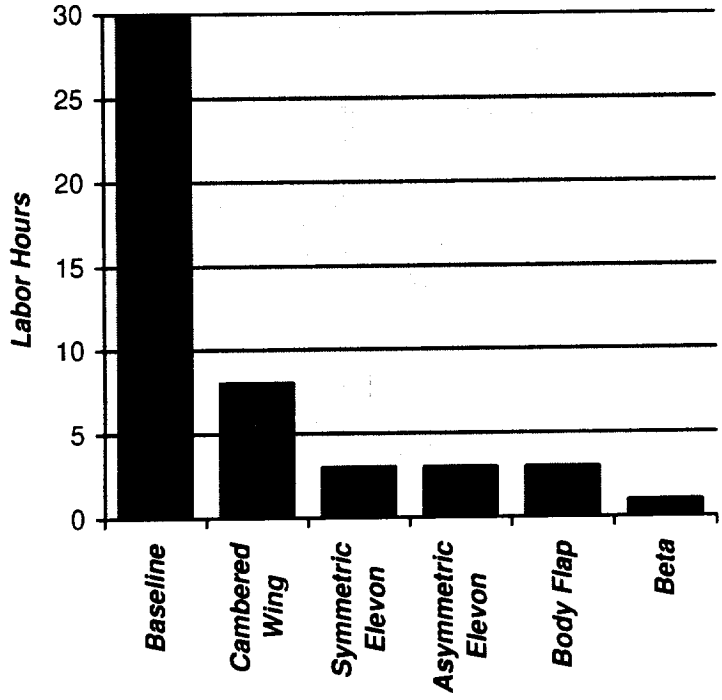

Figure 10. Unstructured Grid Labor Hours.

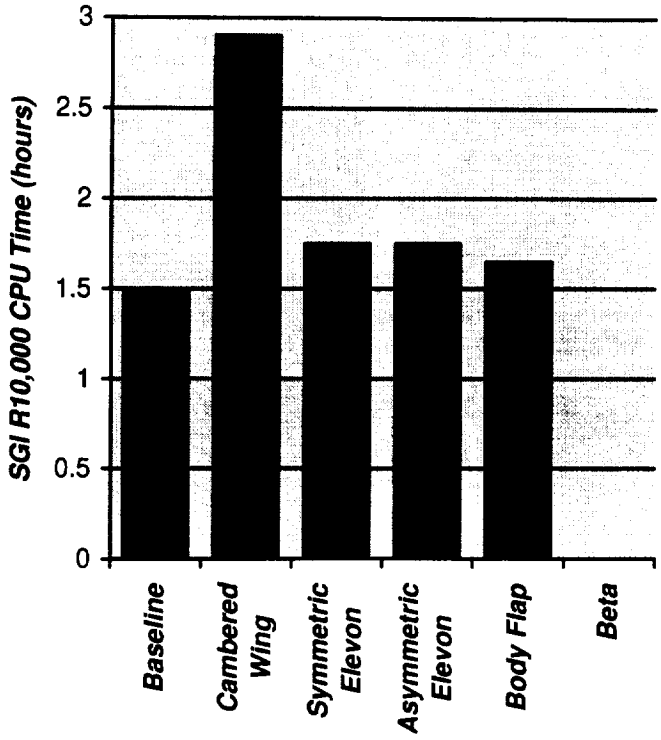

Figure 11. Unstructured Grid Computation Time.

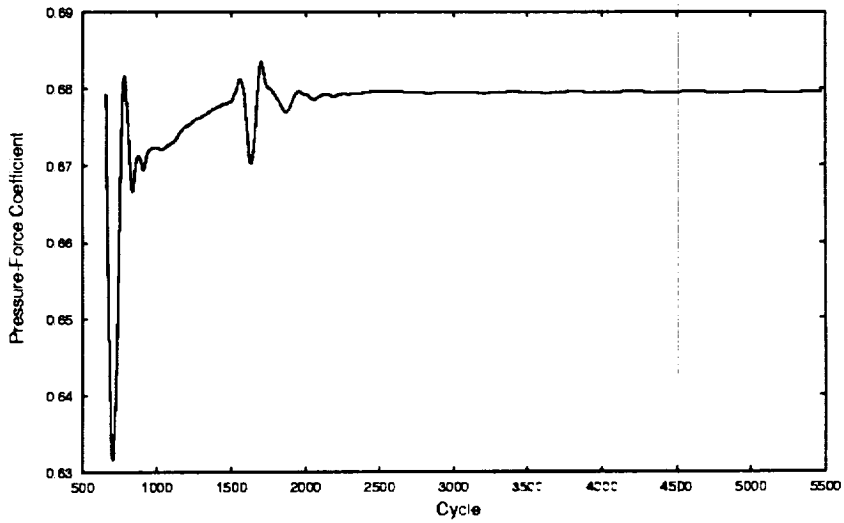

Figure 12. Lift Convergence , Unstructured Grid Euler Solution, Mach 1.2, 10 degrees angle of attack, 5 degrees sideslip.

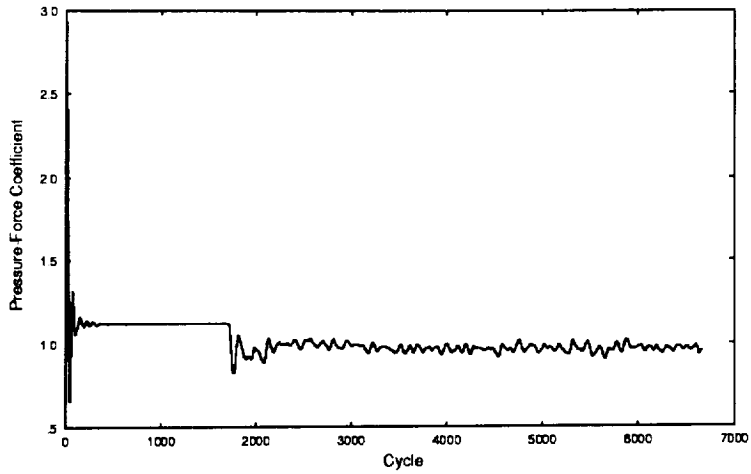

Figure 13. Lift Convergence, Unstructured Grid Euler Solution, Mach 0.6, 20 degrees angle of attack.

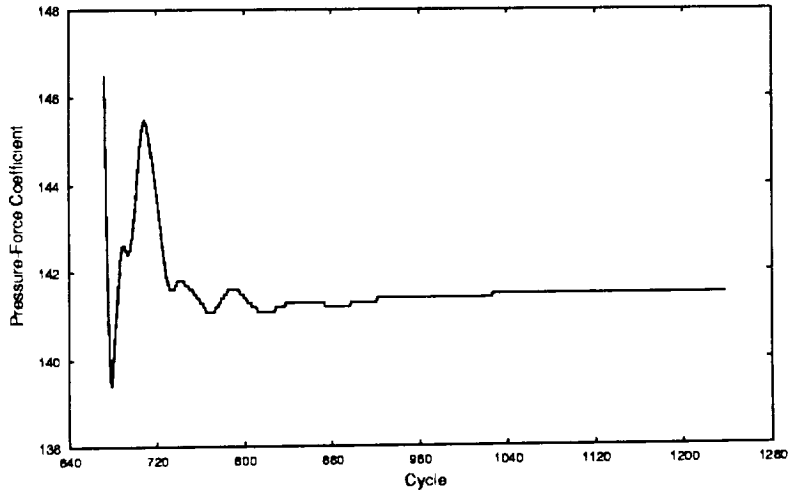

Figure 14. Lift Convergence , Navier-Stokes Solution, Mach 0.6, 10 degrees angle of attack.

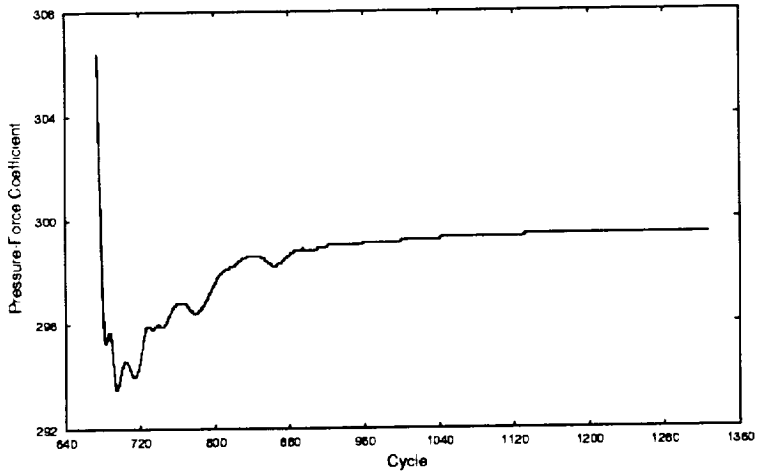

Figure 15. Lift Convergence, Navier-Stokes Solution, Mach 0.6, 20 degrees angle of attack.

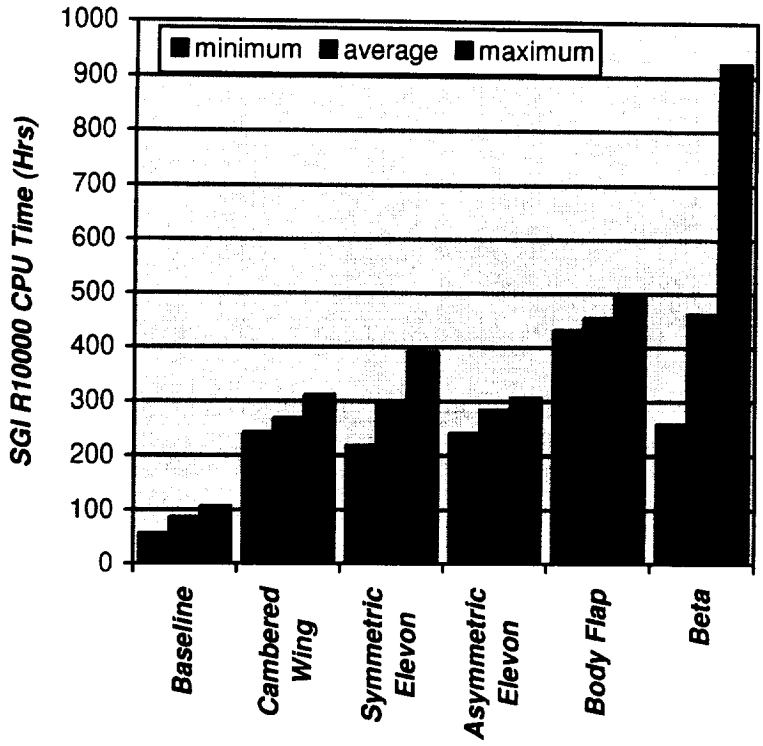

Figure 16. NASTD Euler Solution Computation Times.

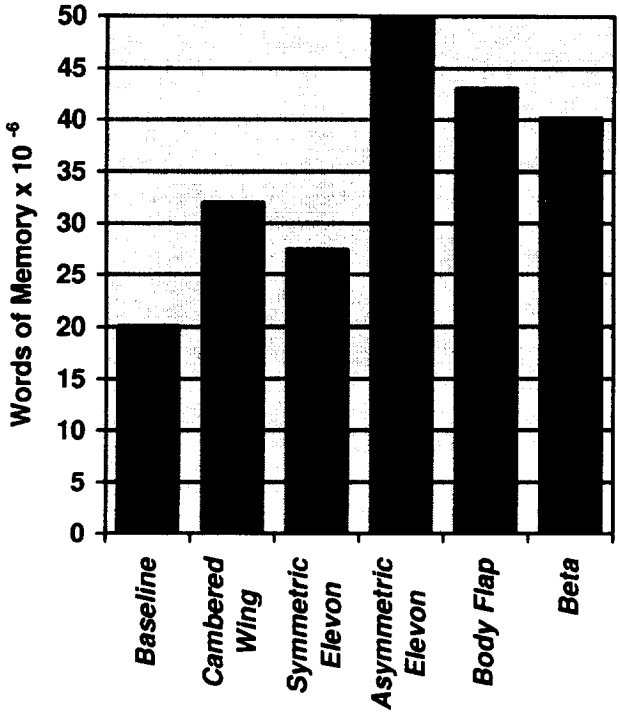

Figure 17. NASTD Euler Solution Memory Requirements.

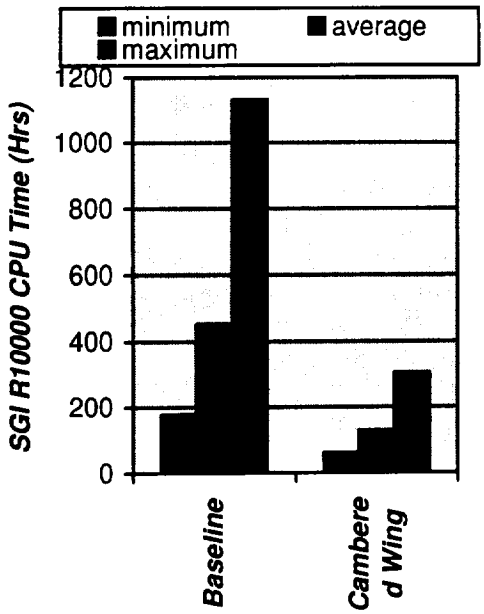

a.) Single Processor Run Time

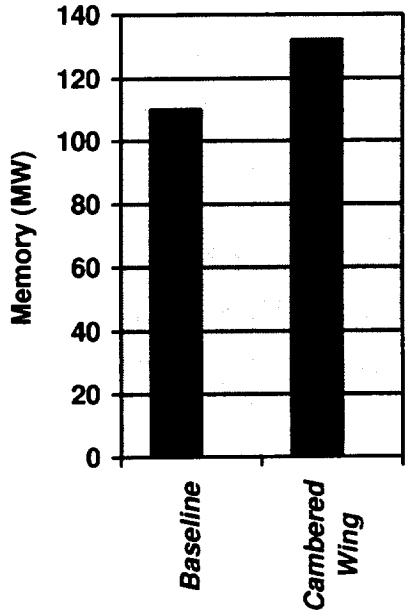

b) Single Processor Memory Requirements

Figure 18. NASTD Navier Stokes Solution Time and Memory Requirements.

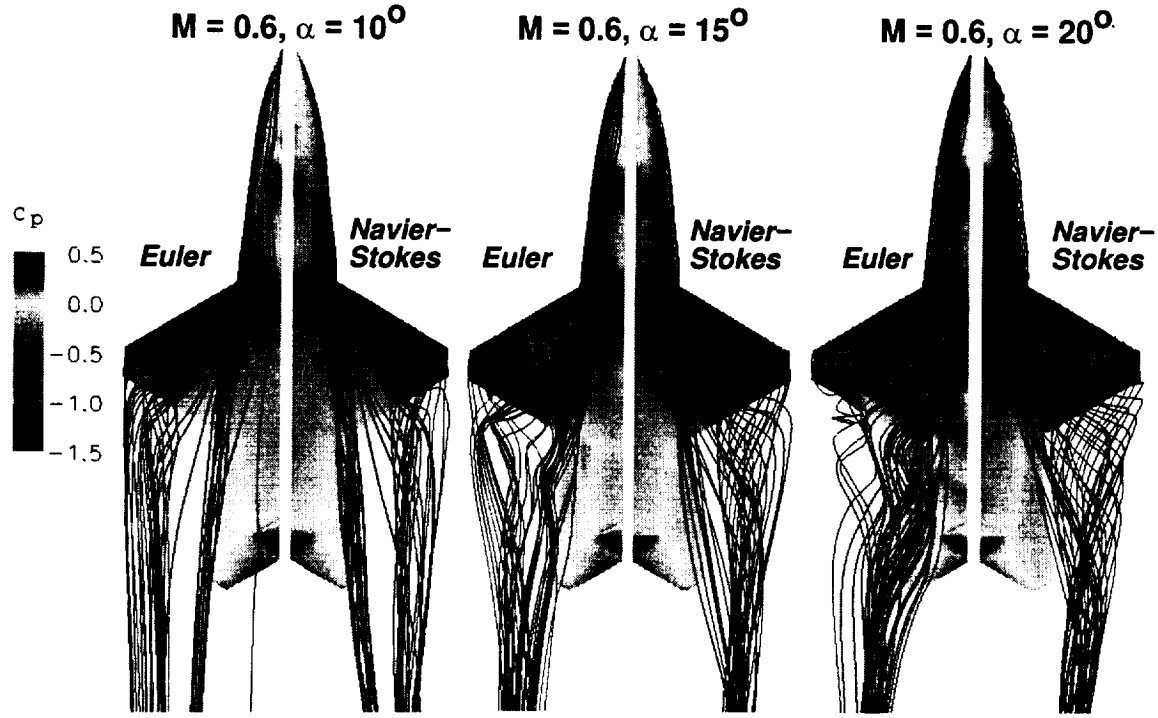

Figure 19. Viscous Effects Versus Angle of Attack, ACWFT Baseline Configuration, Mach 0.6, NASTD Euler and Navier-Stokes Solutions.

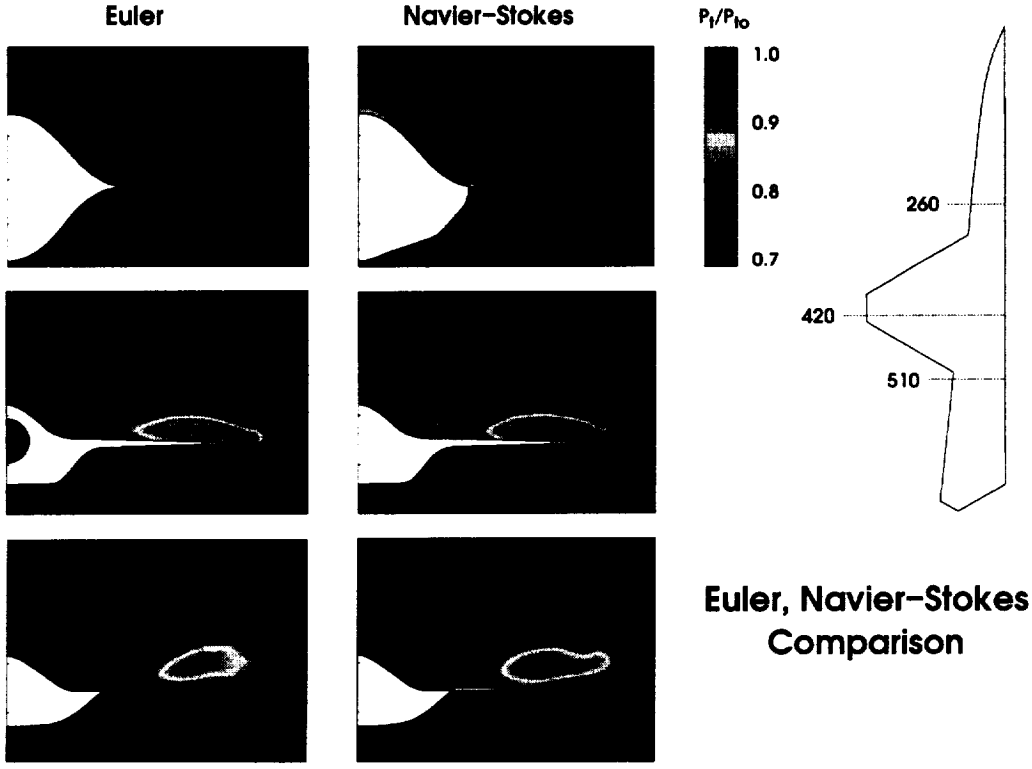

Figure 20. Euler and Navier-Stokes Comparison, Total Pressure Contours, ACWFT Baseline Configuration, Mach 0.6, 10 Degrees Angle of Attack.

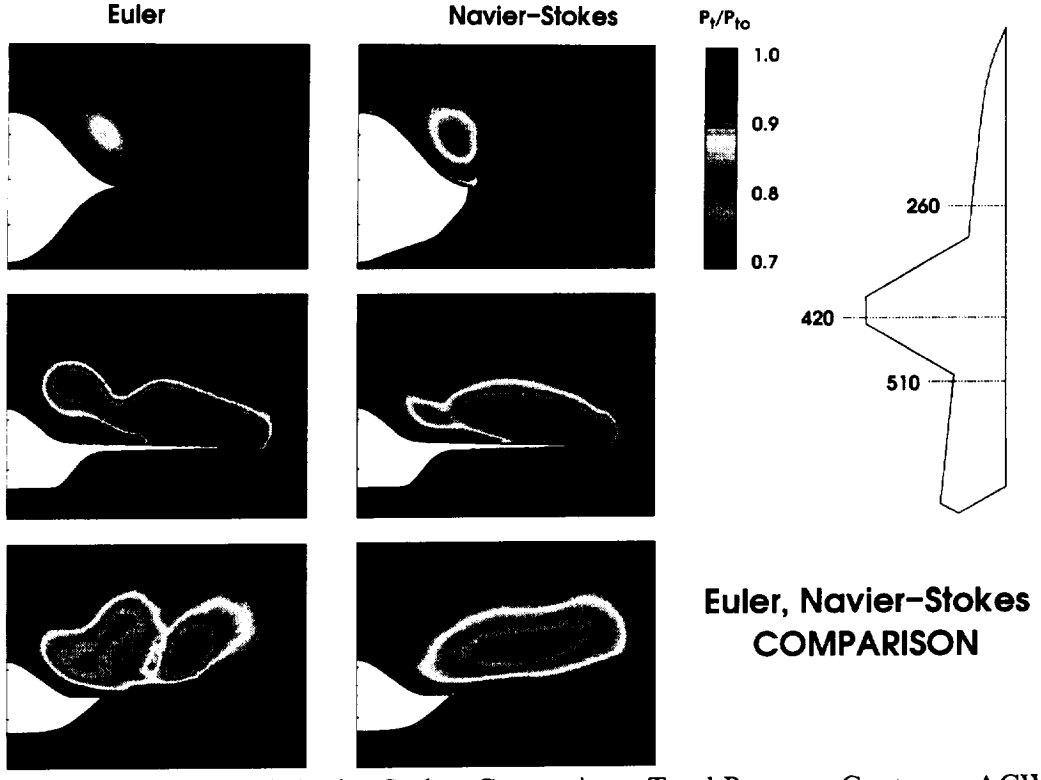

Figure 21. Euler and Navier-Stokes Comparison, Total Pressure Contours, ACWFT Baseline Configuration, Mach 0.6, 20 Degrees Angle of Attack.

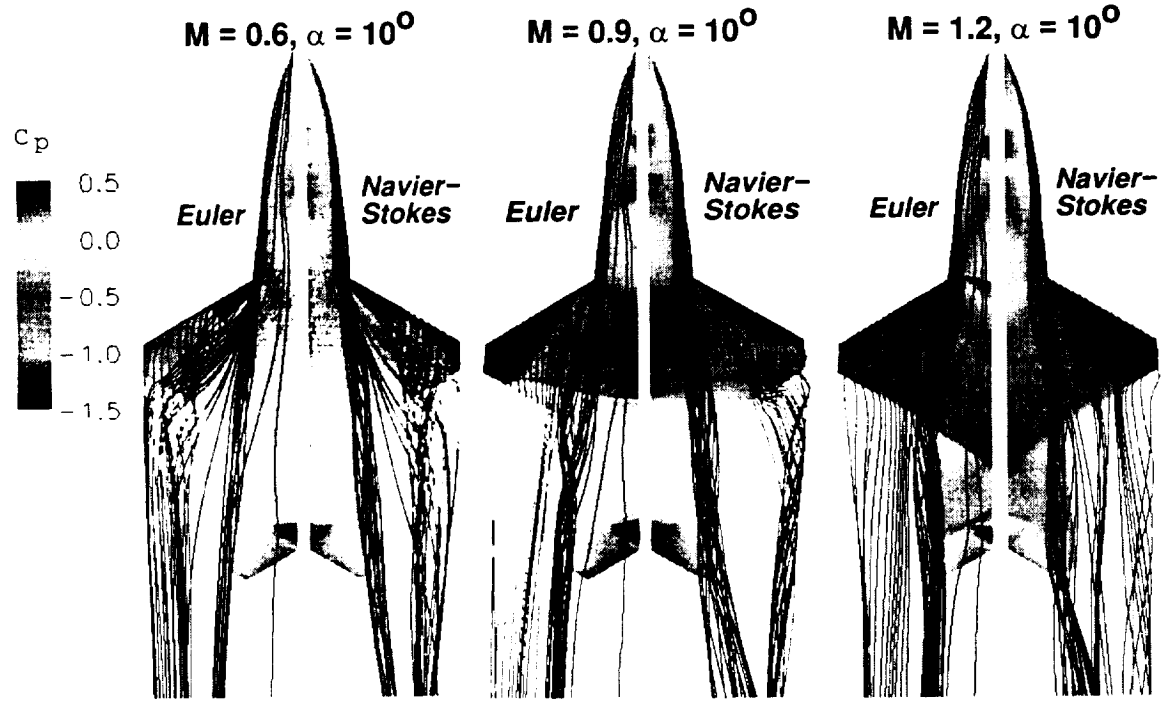

Figure 22. Viscous Effects Versus Mach Number, ACWFT Baseline Configuration, 10 Degrees Angle of Attack, NASTD Euler and Navier-Stokes Solutions.

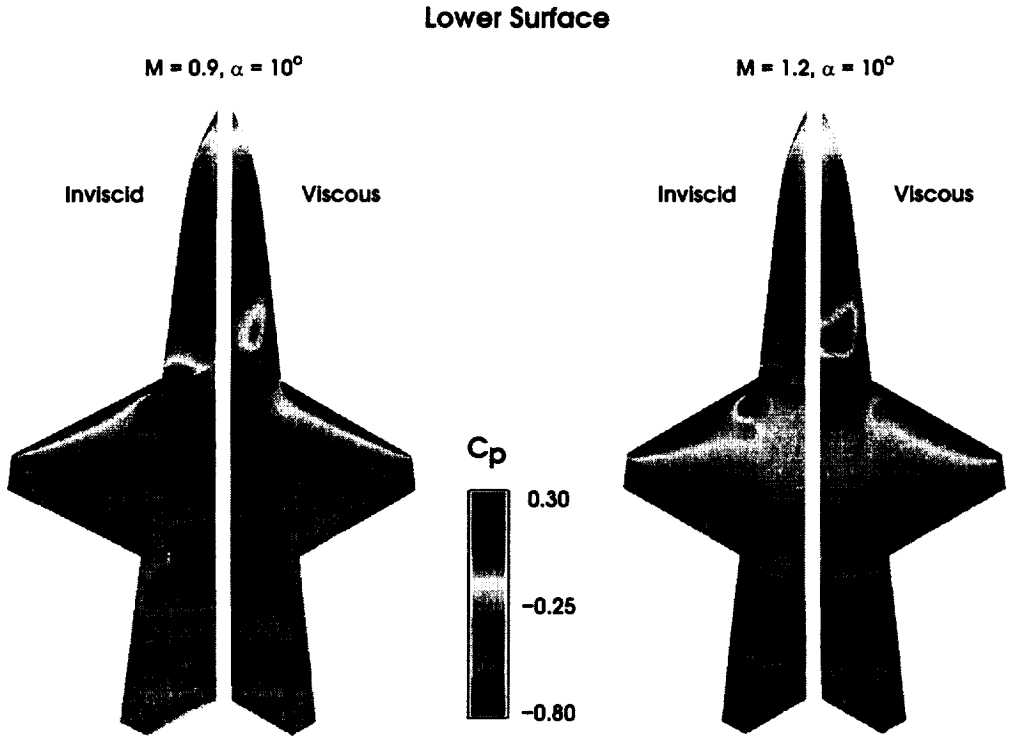

Figure 23. Pressure Coefficient Contours on Lower Surface of ACWFT Baseline Configuration, Euler and Navier-Stokes Solutions.

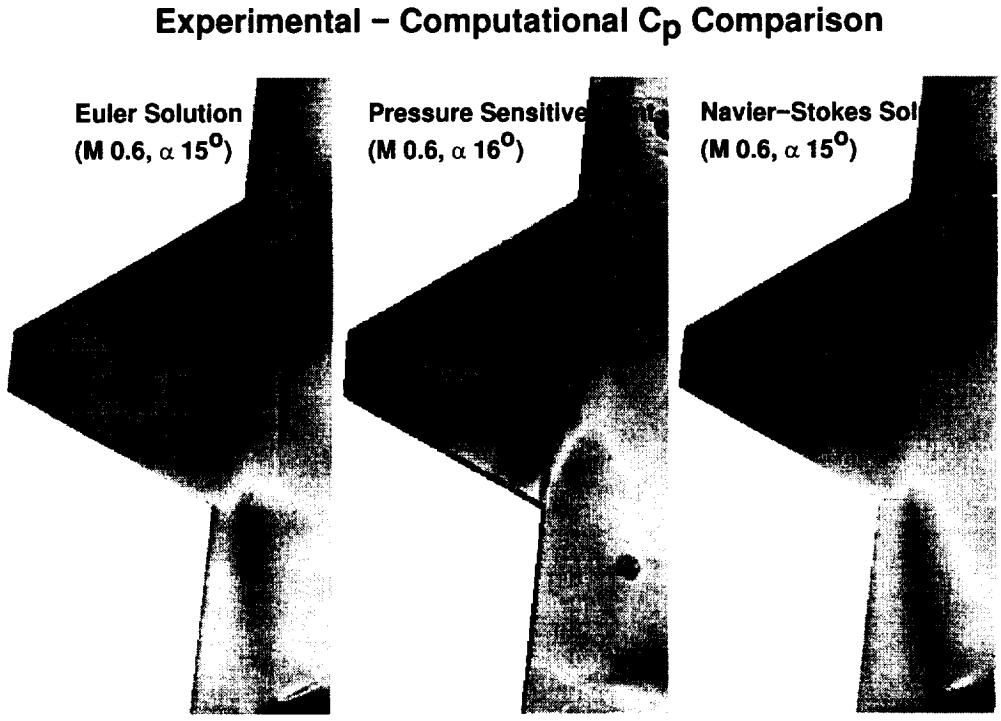

Figure 24. CFD Surface Pressure Comparison With Pressure Sensitive Paint Test Data, ACWFT Baseline Configuration, Mach 0.6, 15 Degrees Angle of Attack.

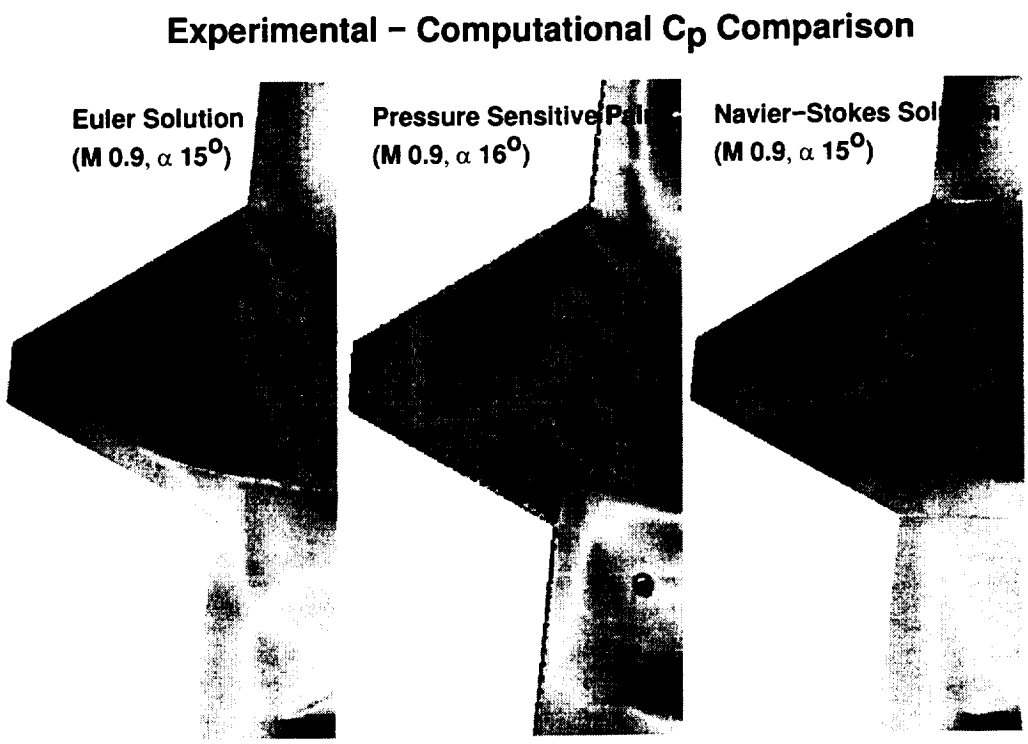

Figure 25. CFD Surface Pressure Comparison With Pressure Sensitive Paint Test Data, ACWFT Baseline Configuration, Mach 0.9, 15 Degrees Angle of Attack.

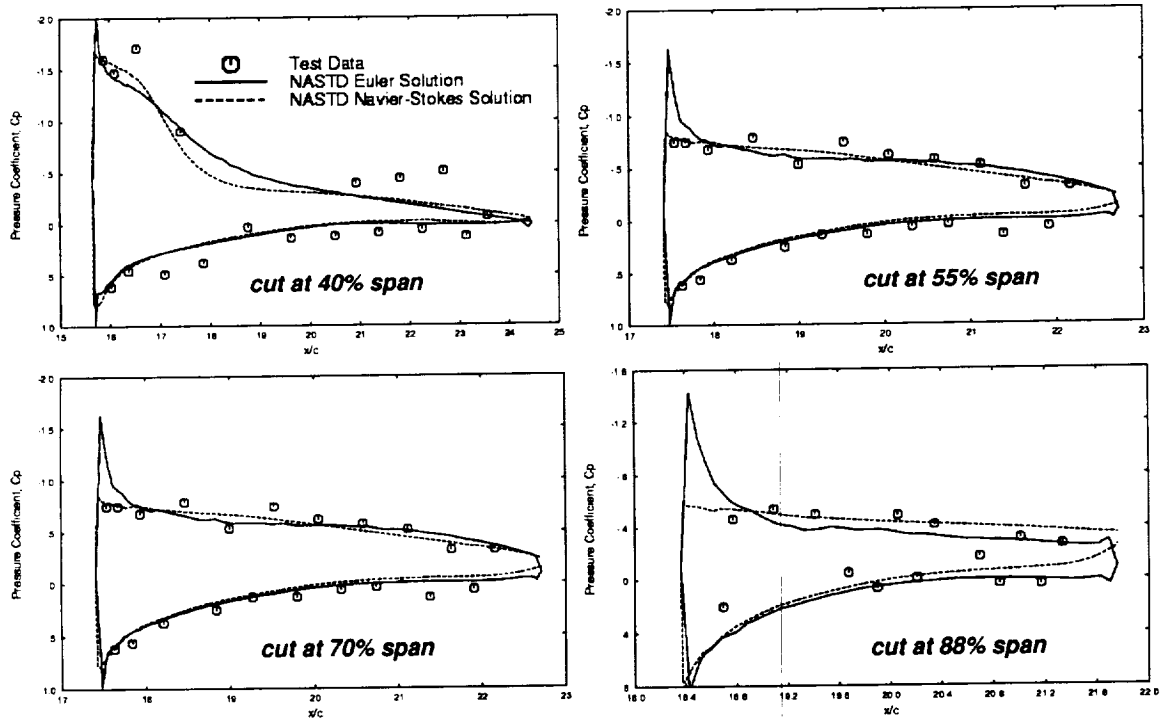

Figure 26. CFD Surface Pressure Comparison With Test Data, ACWFT Baseline Configuration, Mach 0.6, 10 Degrees Angle of Attack.

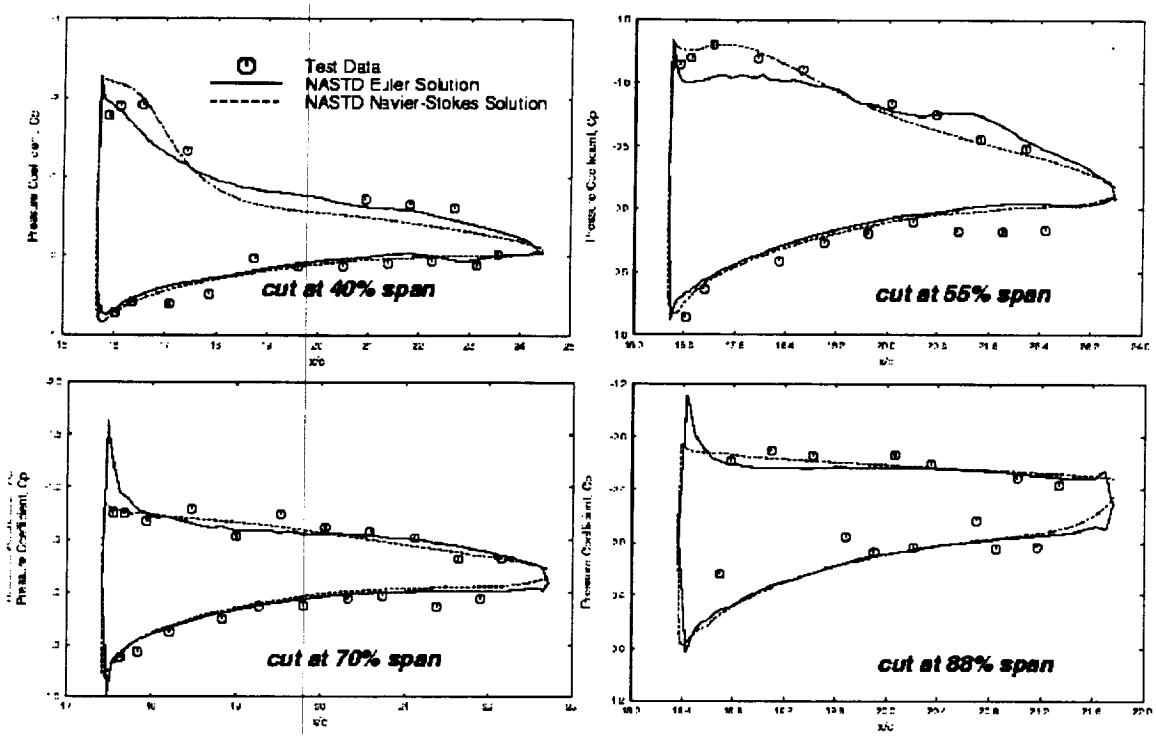

Figure 27. CFD Surface Pressure Comparison With Test Data, ACWFT Baseline Configuration, Mach 0.6, 15 Degrees Angle of Attack.

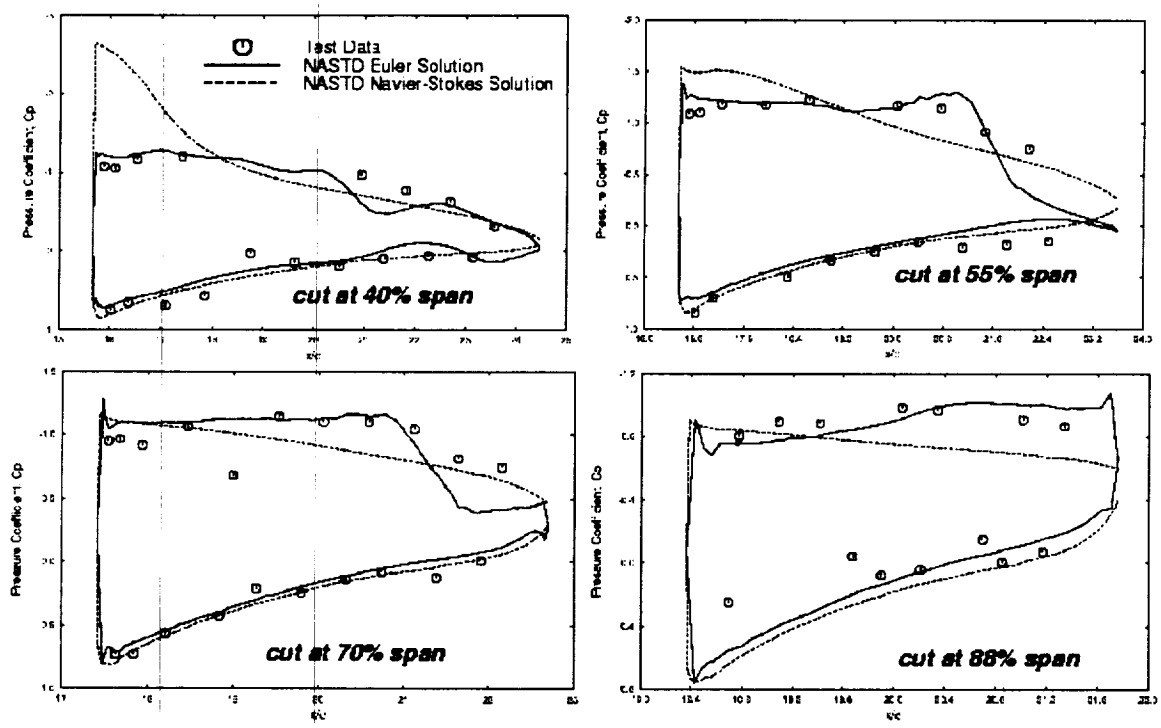

Figure 28. CFD Surface Pressure Comparison With Test Data, ACWFT Baseline Configuration, Mach 0.6, 20 Degrees Angle of Attack.

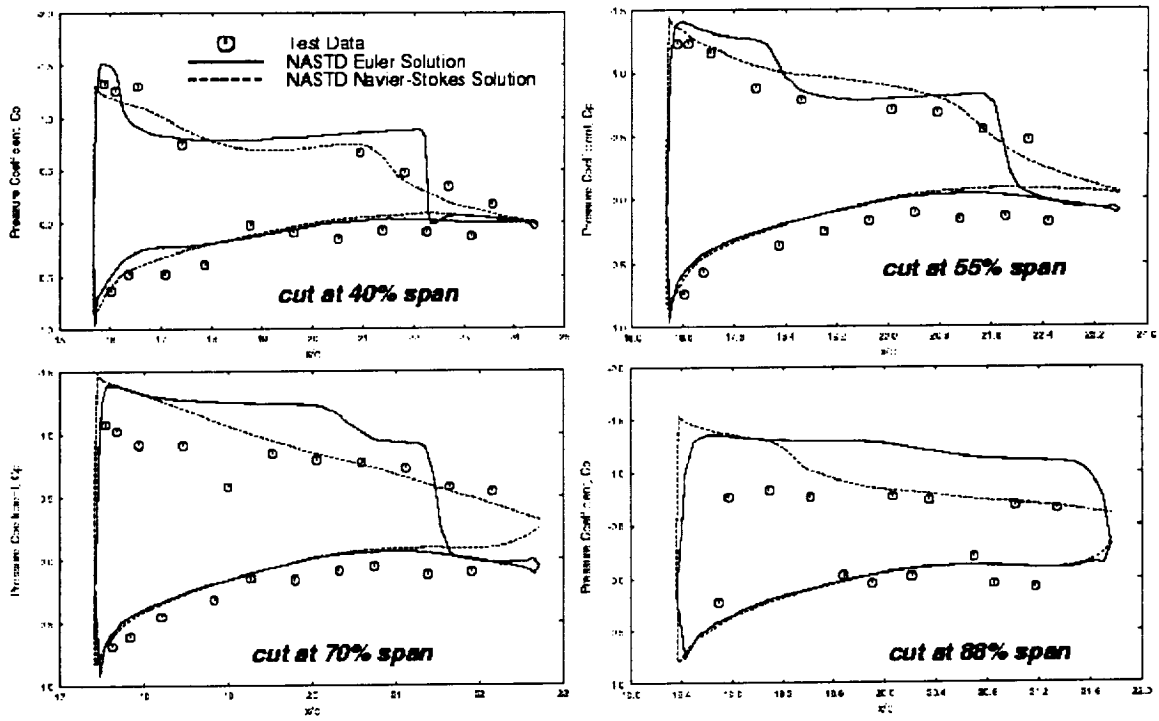

Figure 29. CFD Surface Pressure Comparison With Test Data, ACWFT Baseline Configuration, Mach 0.9, 10 Degrees Angle of Attack.

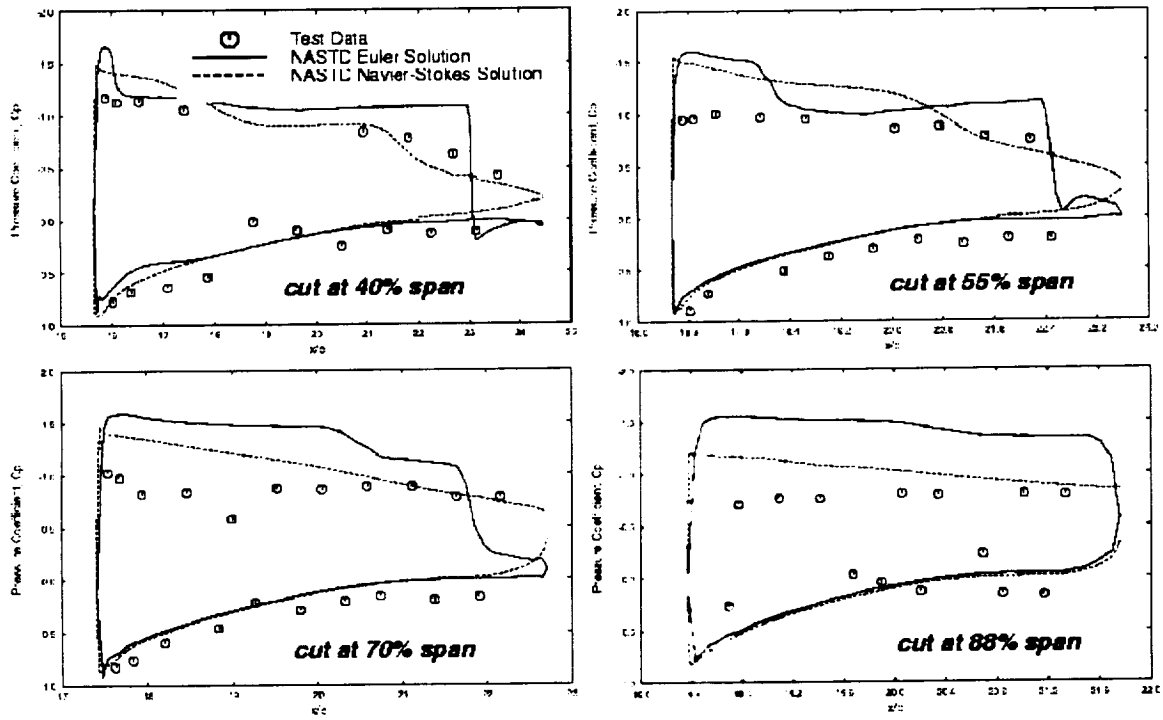

Figure 30. CFD Surface Pressure Comparison With Test Data, ACWFT Baseline Configuration, Mach 0.9, 15 Degree Angle of Attack.

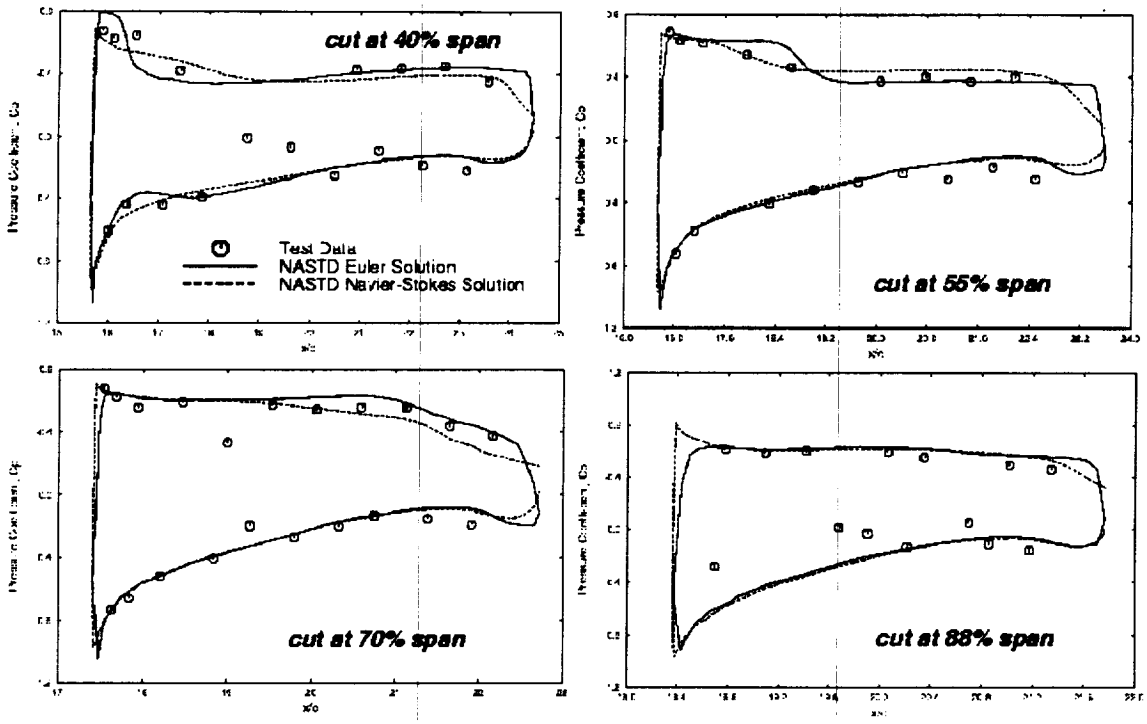

Figure 31. CFD Surface Pressure Comparison With Test Data, ACWFT Baseline Configuration, Mach 1.2, 10 Degrees Angle of Attack.

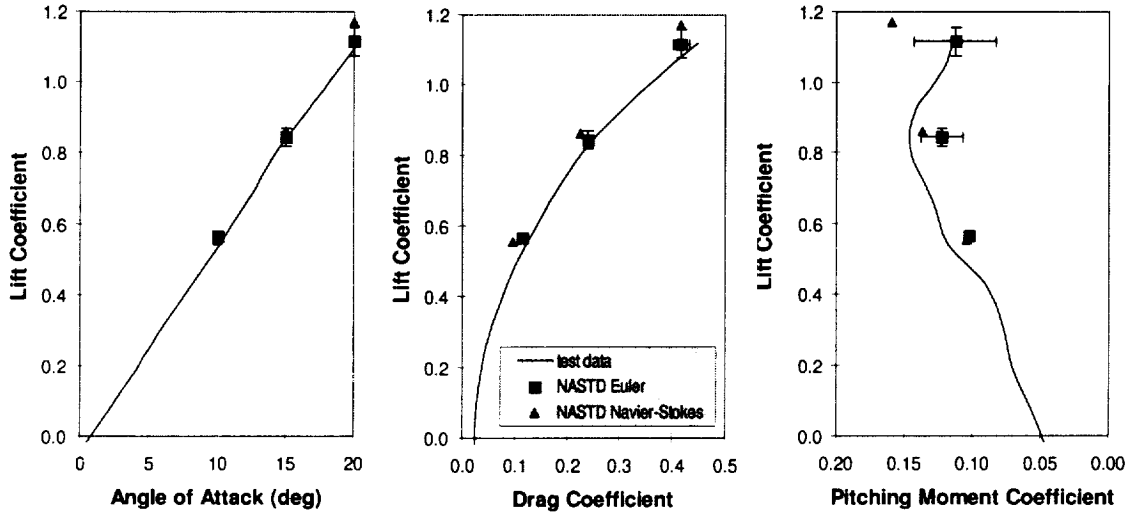

Figure 32. CFD Force and Moment Comparisons With Test Data, ACWFT Baseline Configuration, Mach 0.6.

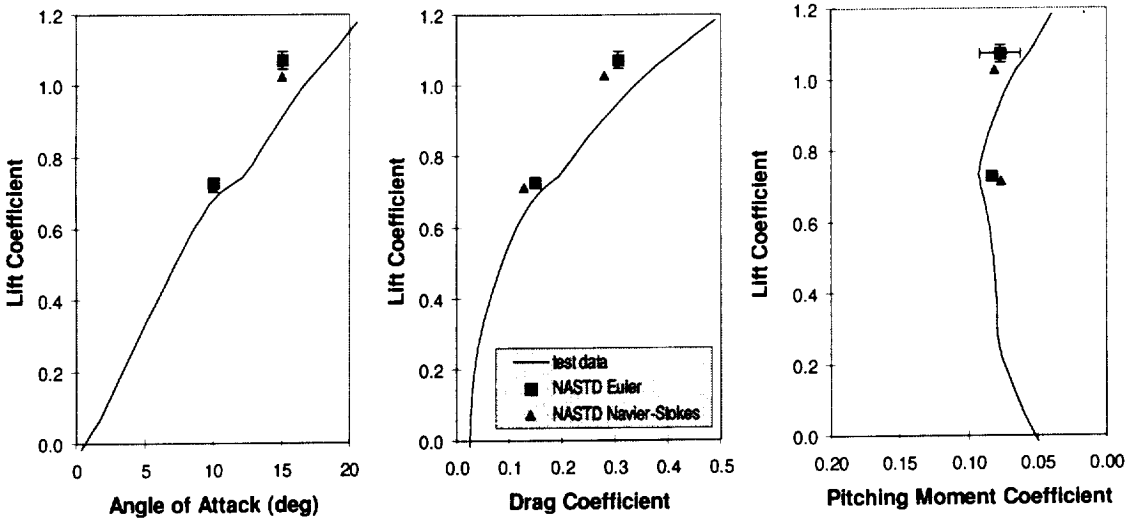

Figure 33. CFD Force and Moment Comparisons With Test Data, ACWFT Baseline Configuration, Mach 0.9.

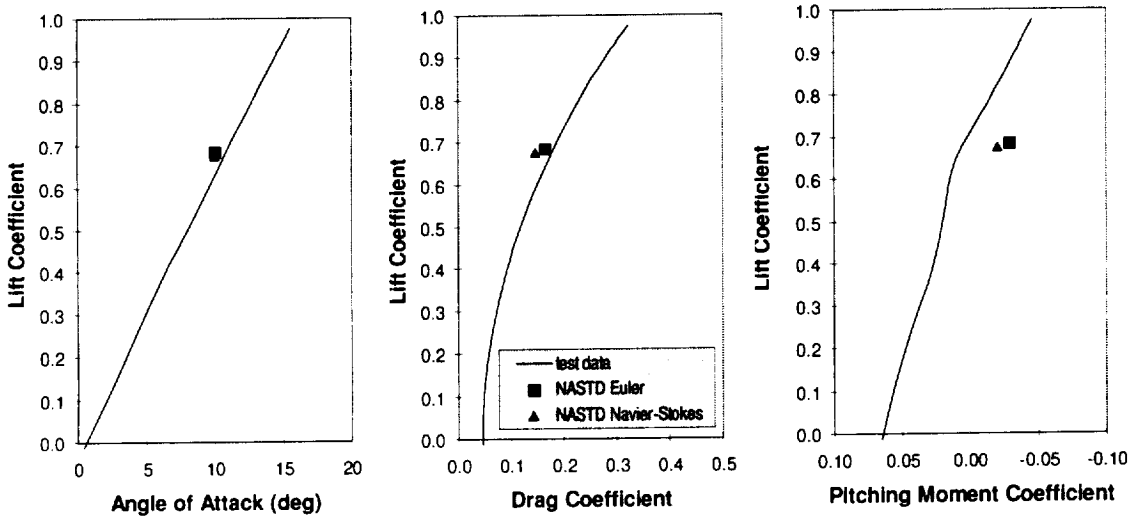

Figure 34. CFD Force and Moment Comparisons With Test Data, ACWFT Baseline Configuration, Mach 1.2.

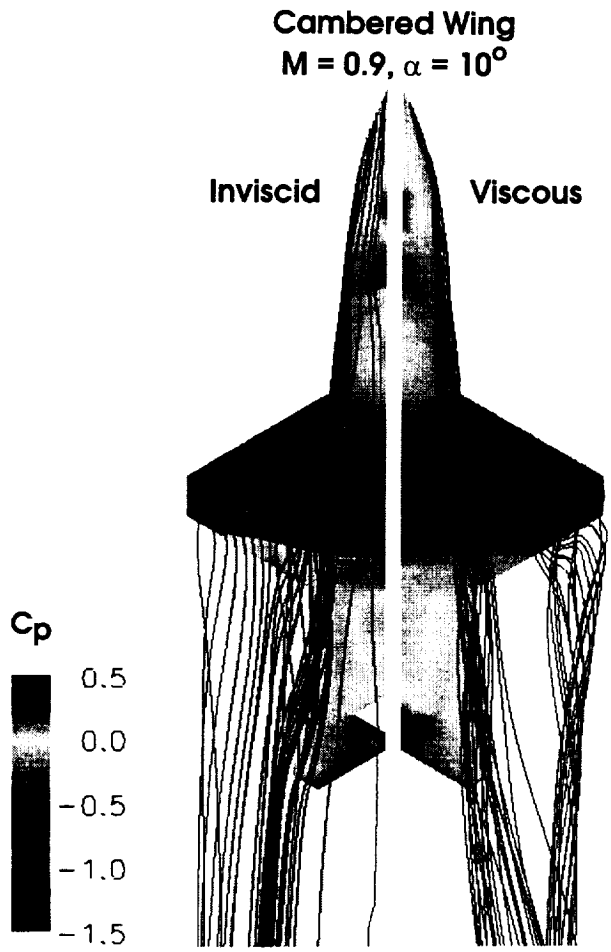

Figure 35. Cambered Wing Surface Pressure Coefficient and Streamline Traces, Mach 0.9, 10 Degrees Angle of Attack.

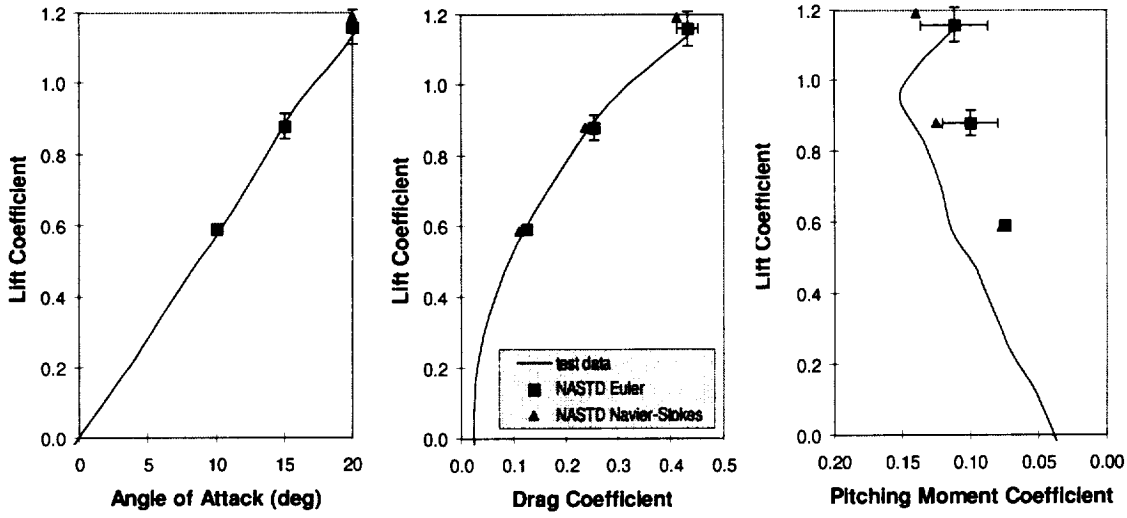

Figure 36. CFD Force and Moment Comparisons With Test Data, ACWFT Cambered Wing Configuration, Mach 0.6.

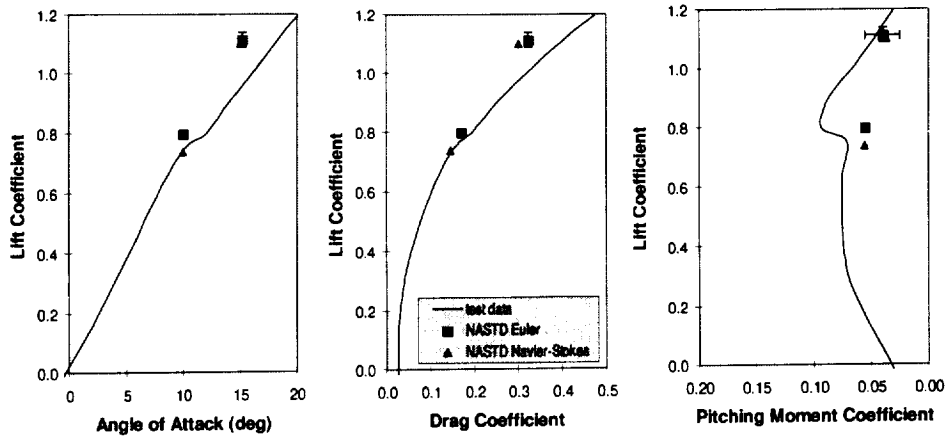

Figure 37. CFD Force and Moment Comparisons With Test Data, ACWFT CamberedWing Configuration, Mach 0.9.

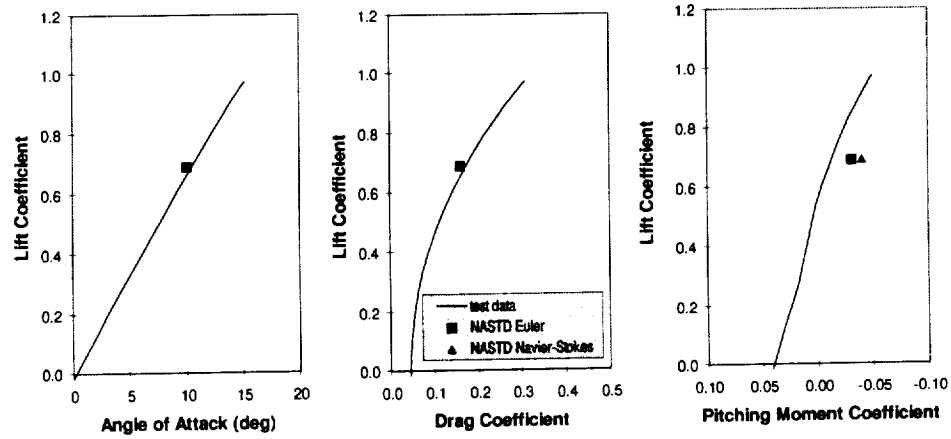

Figure 38. CFD Force and Moment Comparisons With Test Data, ACWFT Cambered Wing Configuration, Mach 1.2.

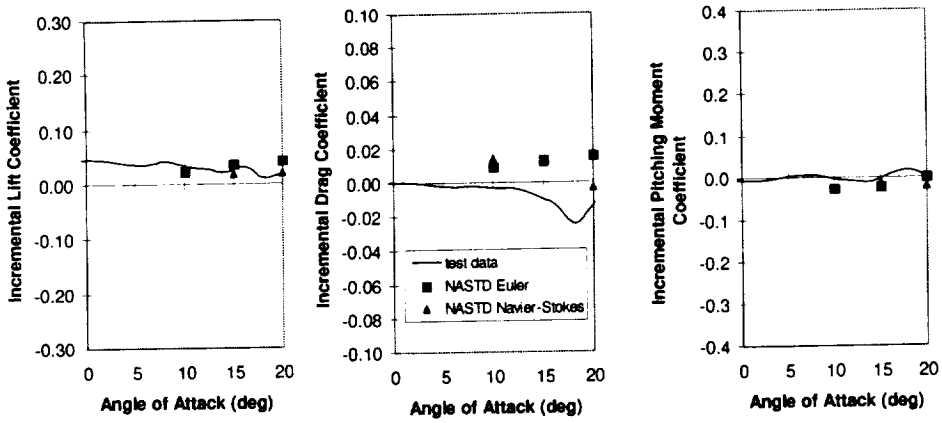

Figure 39. CFD Incremental Force and Moment Comparisons With Test Data, ACWFT Cambered Wing Configuration, Mach 0.6.

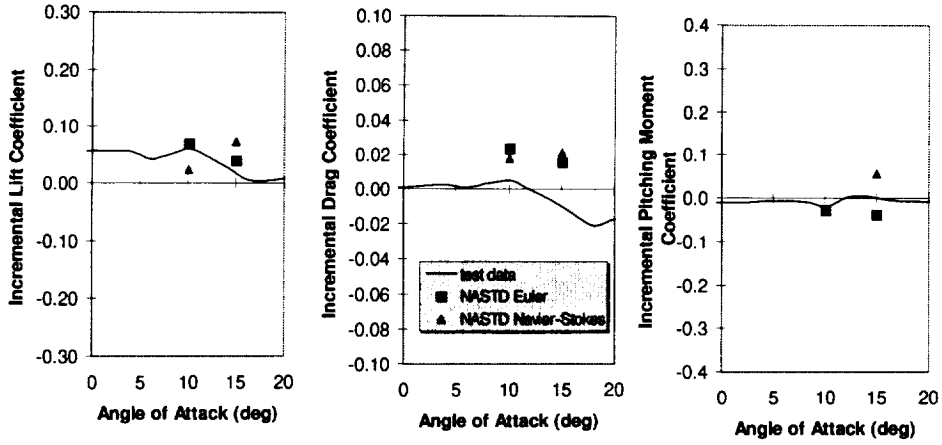

Figure 40. CFD Incremental Force and Moment Comparisons With Test Data, ACWFT Cambered Wing Configuration, Mach 0.9.

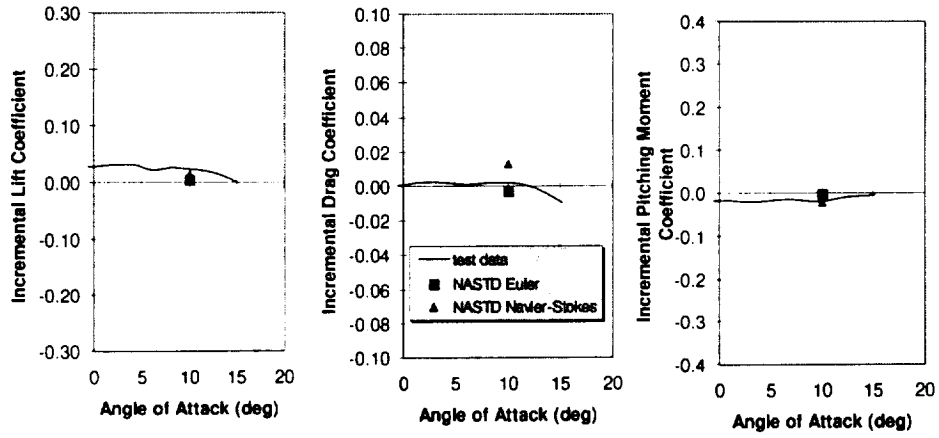

Figure 41. CFD Incremental Force and Moment Comparisons With Test Data, ACWFT Cambered Wing Configuration, Mach 1.2.

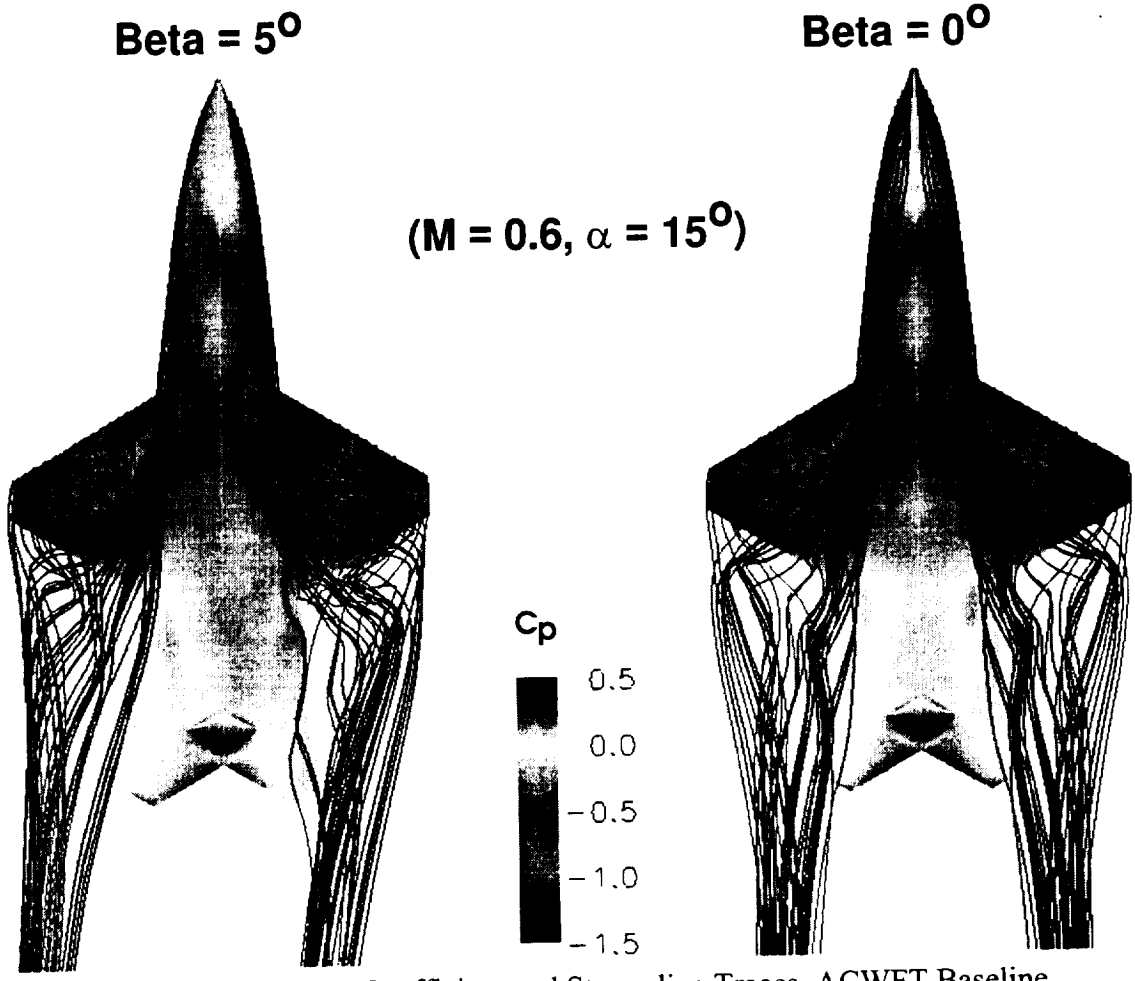

Figure 42. Surface Pressure Coefficient and Streamline Traces, ACWFT Baseline Configuration, Mach 0.6, 0 and 5 Degrees Side Slip Angles, 15 Degrees Angle of Attack.

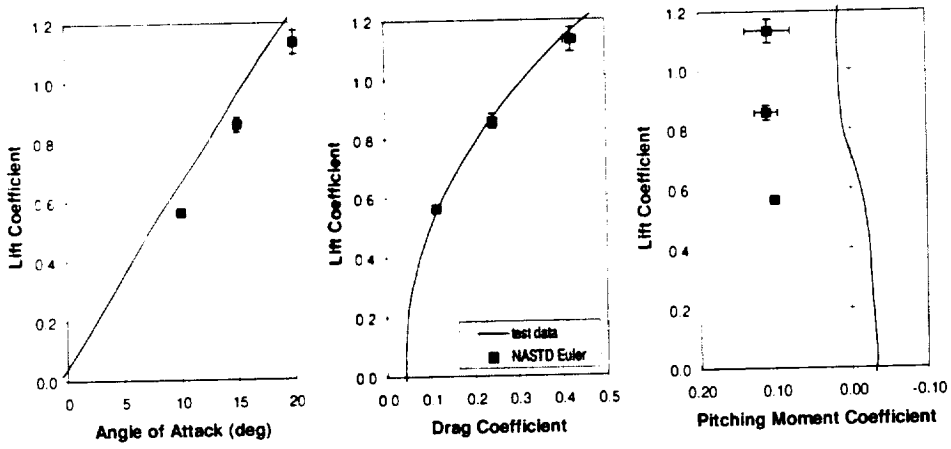

Figure 43. CFD Force and Moment Comparisons With Test Data, ACWFT Baseline Configuration, 5 Degrees Sideslip, Mach 0.6.

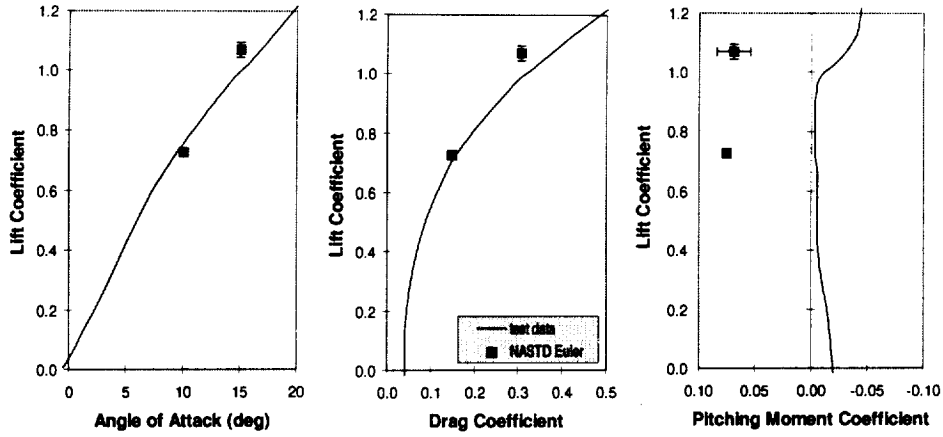

Figure 44. CFD Force and Moment Comparisons With Test Data, ACWFT Baseline Configuration, 5 Degrees Sideslip, Mach 0.9.

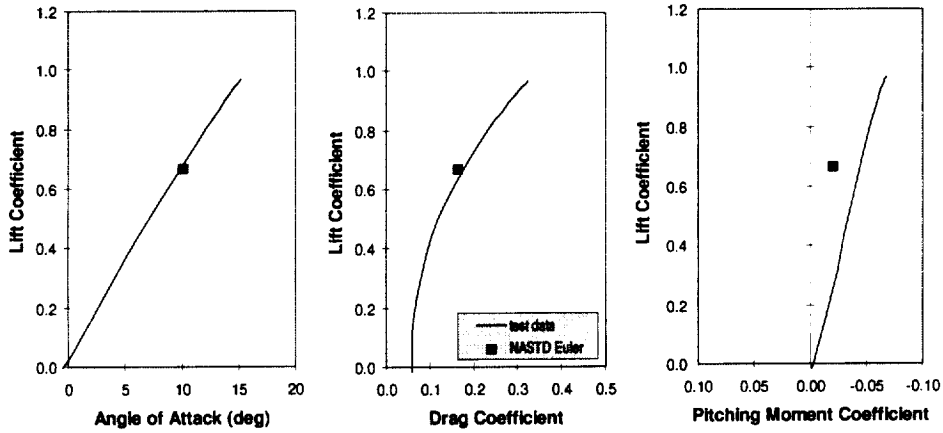

Figure 45. CFD Force and Moment Comparisons With Test Data, ACWFT Baseline Configuration, 5 Degrees Sideslip, Mach 1.2.

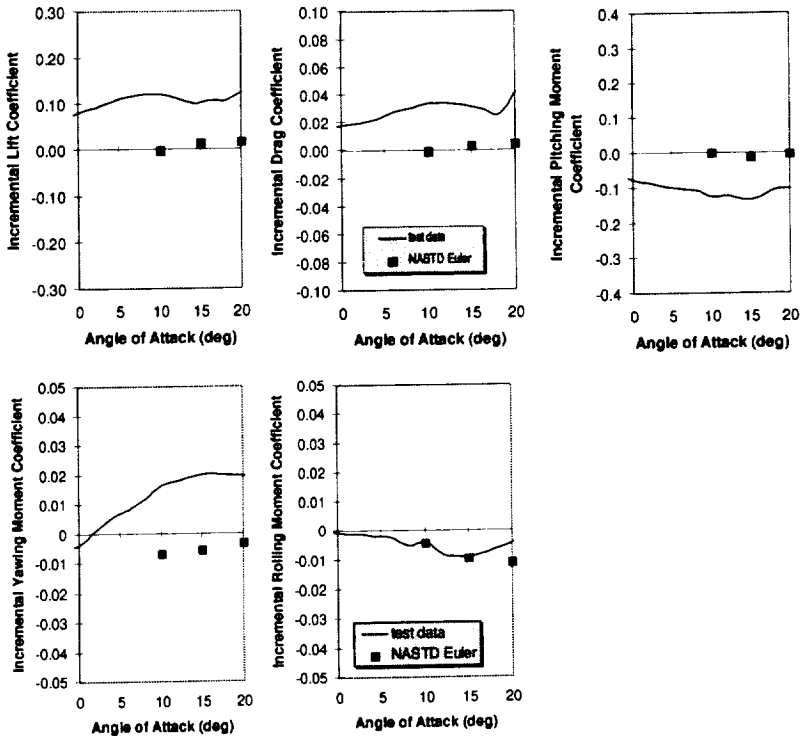

Figure 46. CFD Incremental Force and Moment Comparisons With Test Data, ACWFT Baseline Configuration, 5 Degrees Sideslip, Mach 0.6.

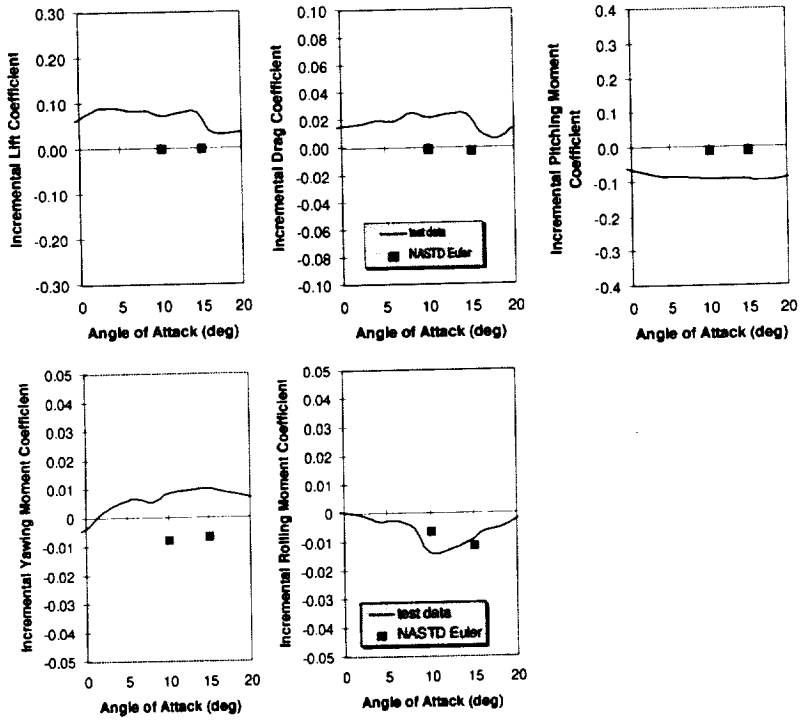

Figure 47. CFD Incremental Force and Moment Comparisons With Test Data, ACWFT Baseline Configuration, 5 Degrees Sideslip, Mach 0.9.

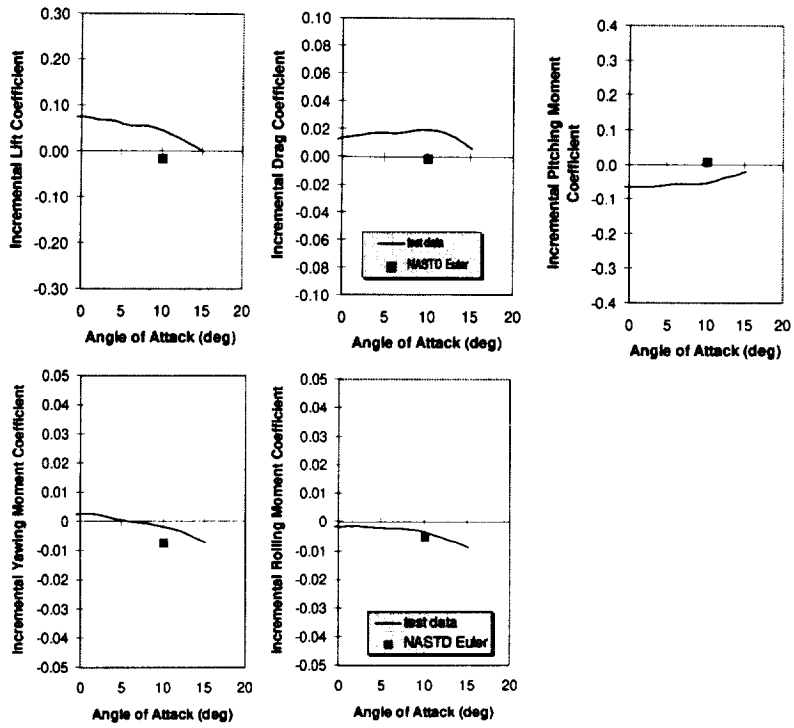

Figure 48. CFD Incremental Force and Moment Comparisons With Test Data, ACWFT Baseline Configuration, 5 Degrees Sideslip, Mach 1.2.

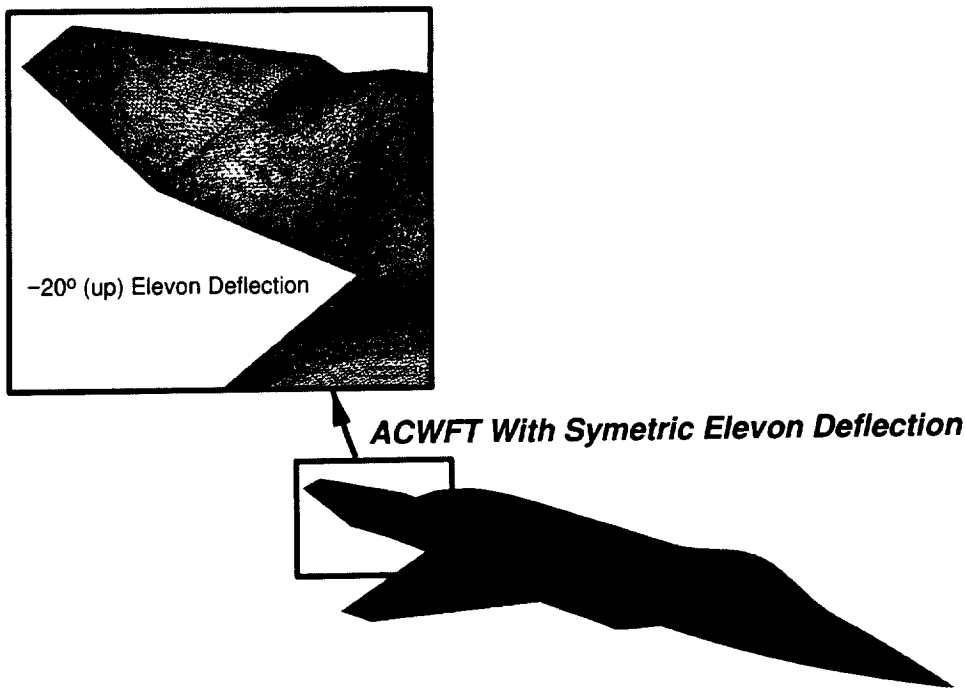

Figure 49. Unstructured Surface Grid About Deflected Elevon.

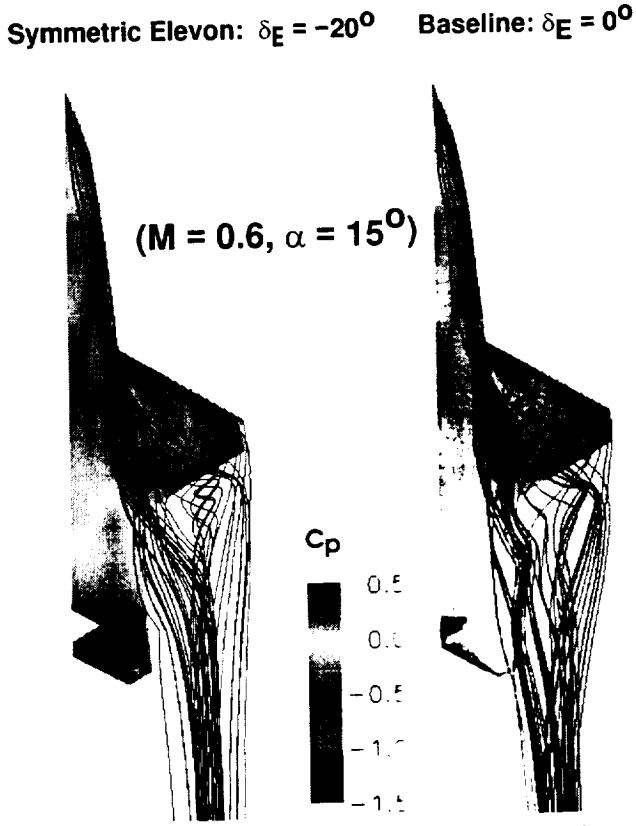

Figure 50. Surface Pressure Coefficient and Streamline Traces for ACWFT Configuration with Symmetric Deflected Elevon Deflections of 0 and -20 Degrees, Mach 0.6, 15 Degrees Angle of Attack.

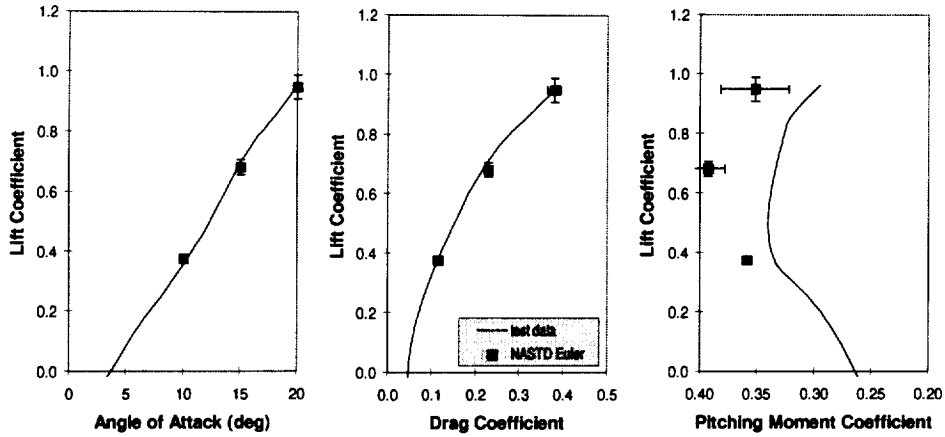

Figure 51. CFD Force and Moment Comparisons With Test Data, ACWFT With -20 Degree Symmetric Elevon Deflection, Mach 0.6.

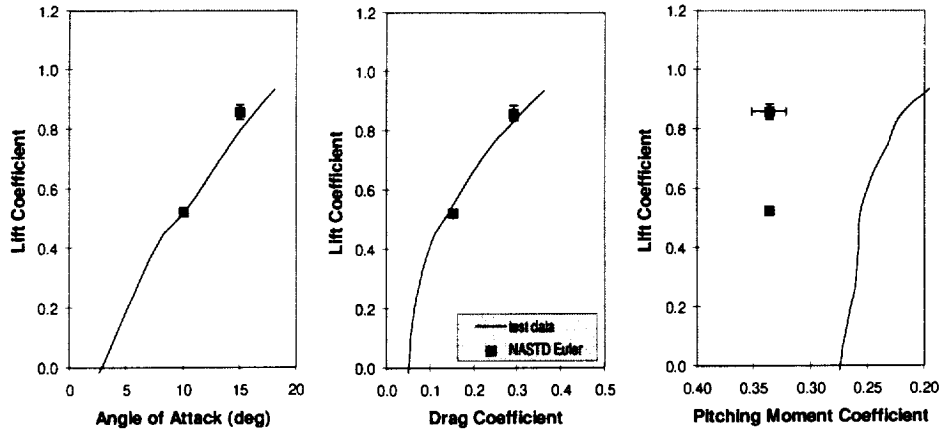

Figure 52. CFD Force and Moment Comparisons With Test Data, ACWFT With -20 Degree Symmetric Elevon Deflection, Mach 0.9.

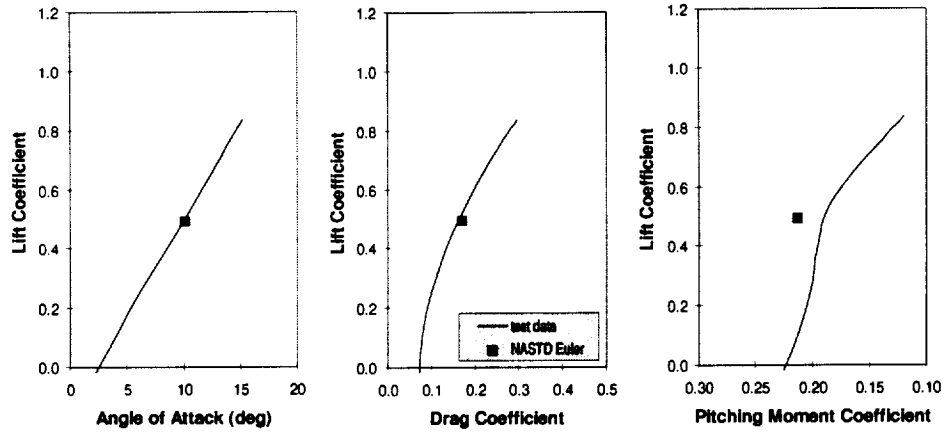

Figure 53. CFD Force and Moment Comparisons With Test Data, ACWFT With -20 Degree Symmetric Elevon Deflection, Mach 1.2.

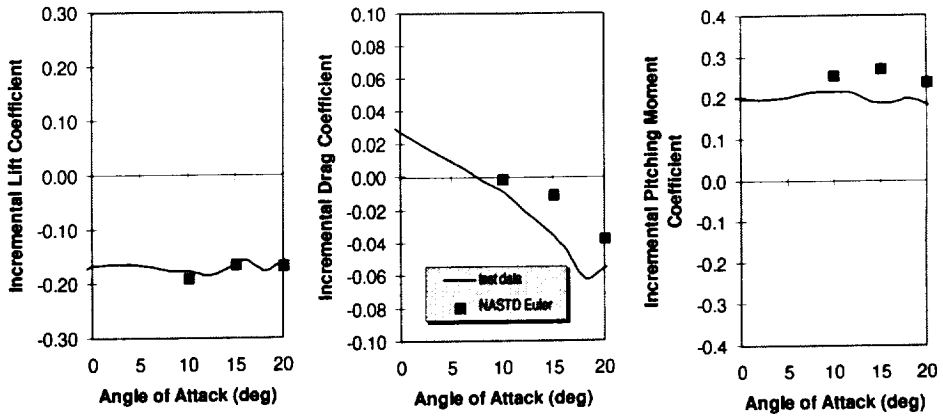

Figure 54. CFD Incremental Force and Moment Comparisons With Test Data, ACWFT With -20 Degree Symmetric Elevon Deflection, Mach 0.6.

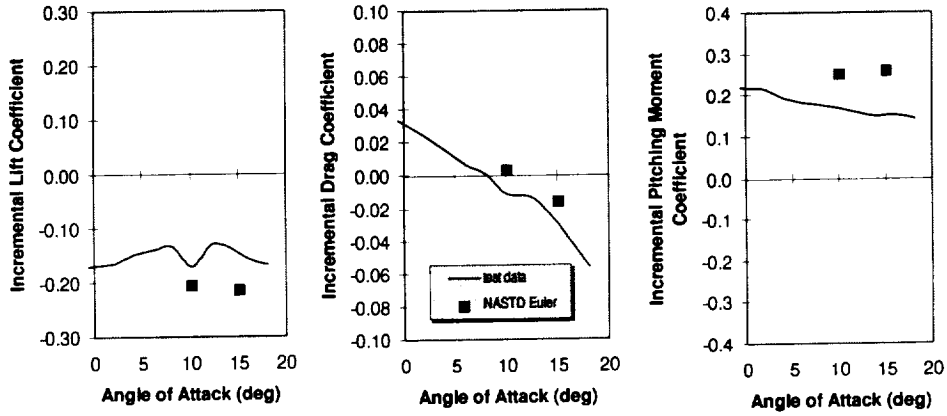

Figure 55. CFD Incremental Force and Moment Comparisons With Test Data, ACWFT With -20 Degree Symmetric Elevon Deflection, Mach 0.9.

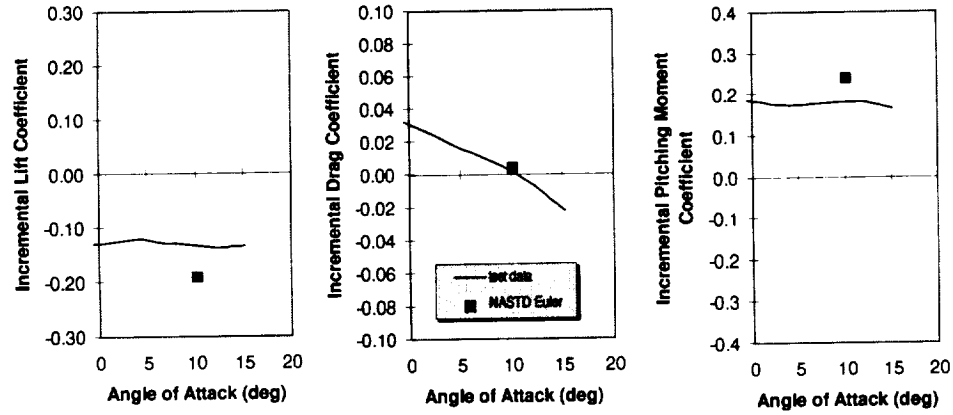

Figure 56. CFD Incremental Force and Moment Comparisons With Test Data, ACWFT With -20 Degree Symmetric Elevon Deflection, Mach 1.2.

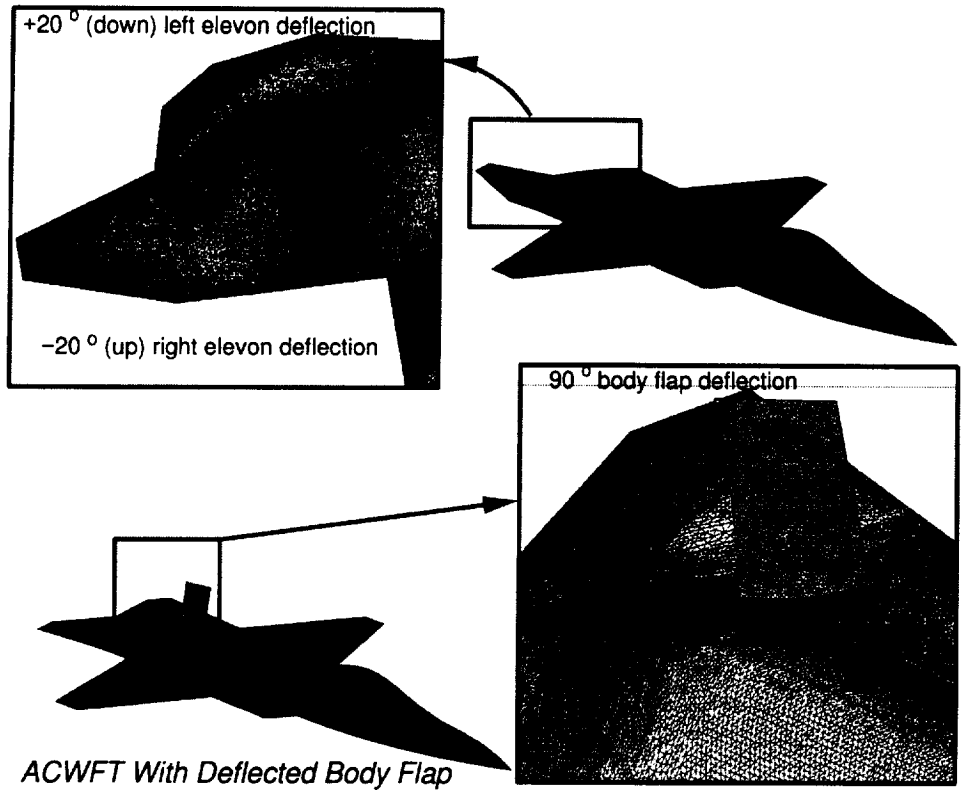

Figure 57. Unstructured Surface Grid About Asymmetrically Deflected Elevon and Deflected Body Flap.

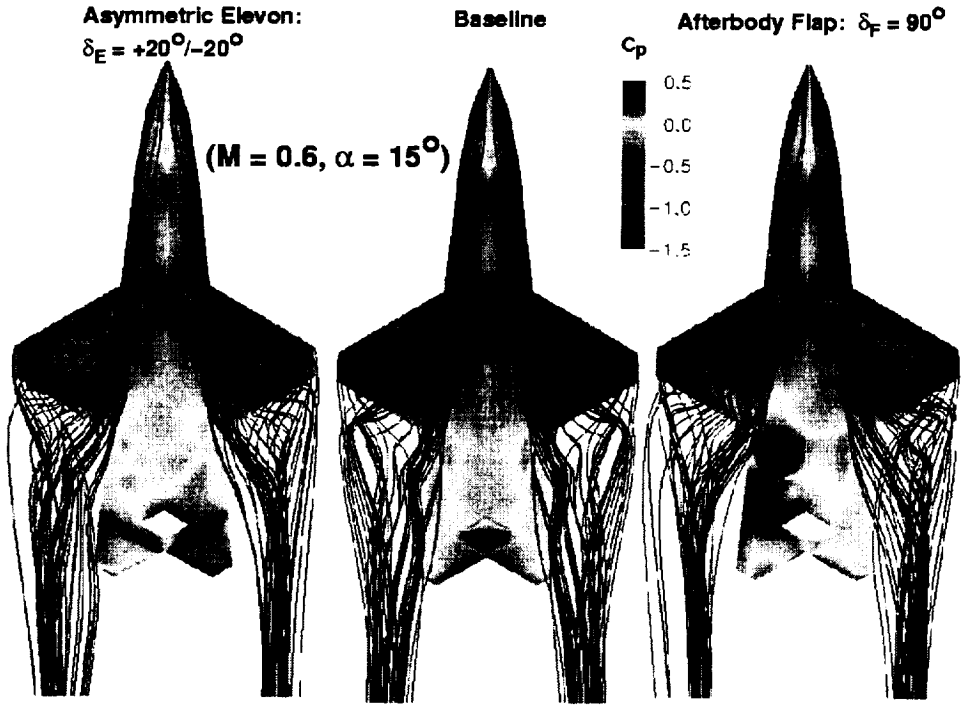

Figure 58. Surface Pressure Coefficient and Streamline Traces, for ACWFT Baseline, Asymmetrically Deflected Elevon, and Deflected Afterbody Flap Configurations, Mach 0.6, 15 Degrees Angle of Attack.

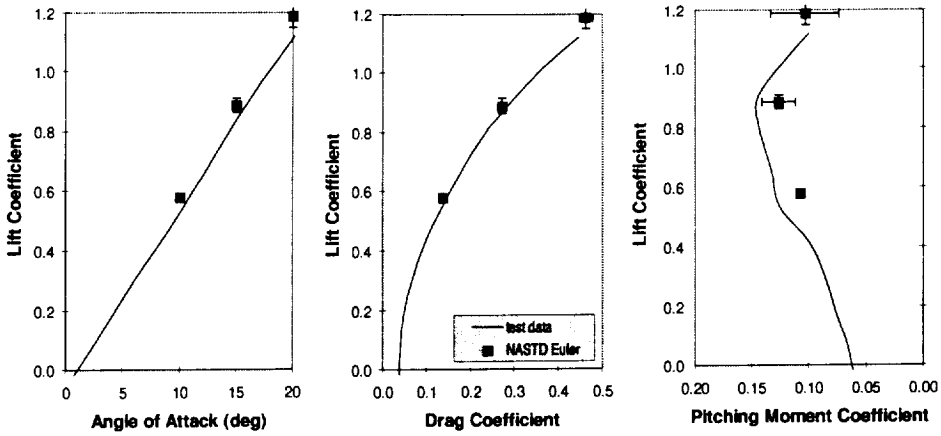

Figure 59. CFD Force and Moment Comparisons With Test Data, ACWFT With Asymmetric Elevon Deflection, Mach 0.6.

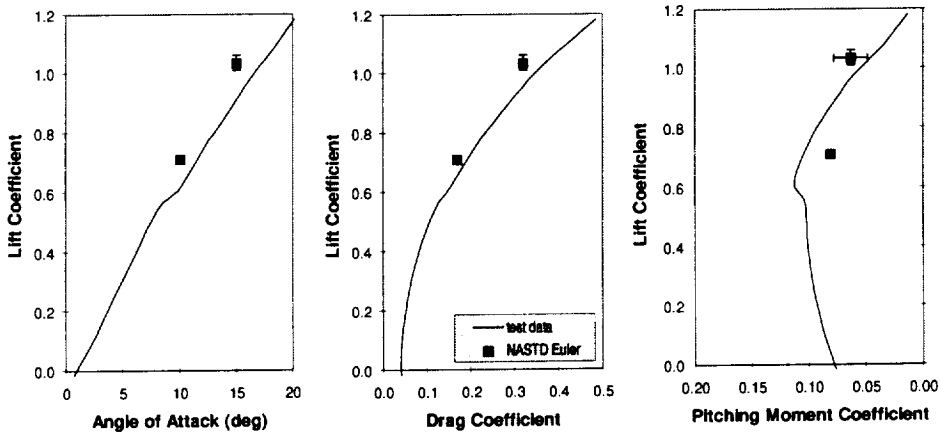

Figure 60. CFD Force and Moment Comparisons With Test Data, ACWFT With Asymmetric Elevon Deflection, Mach 0.9.

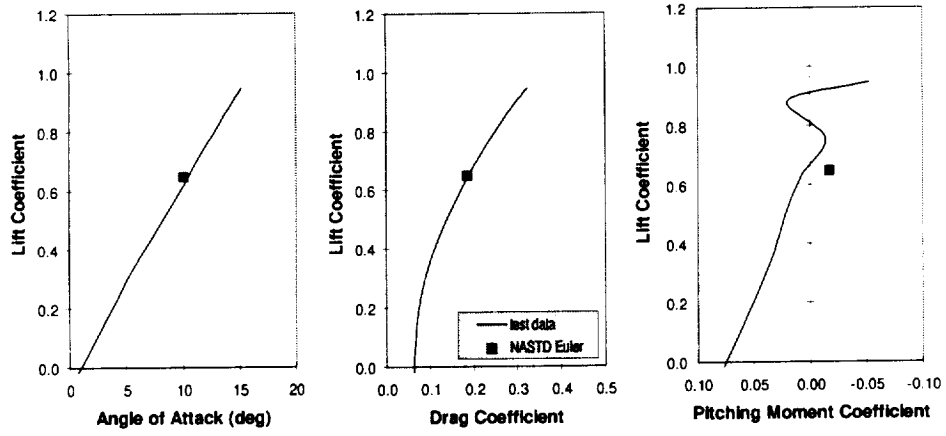

Figure 61. CFD Force and Moment Comparisons With Test Data, ACWFT With Asymmetric Elevon Deflection, Mach 1.2.

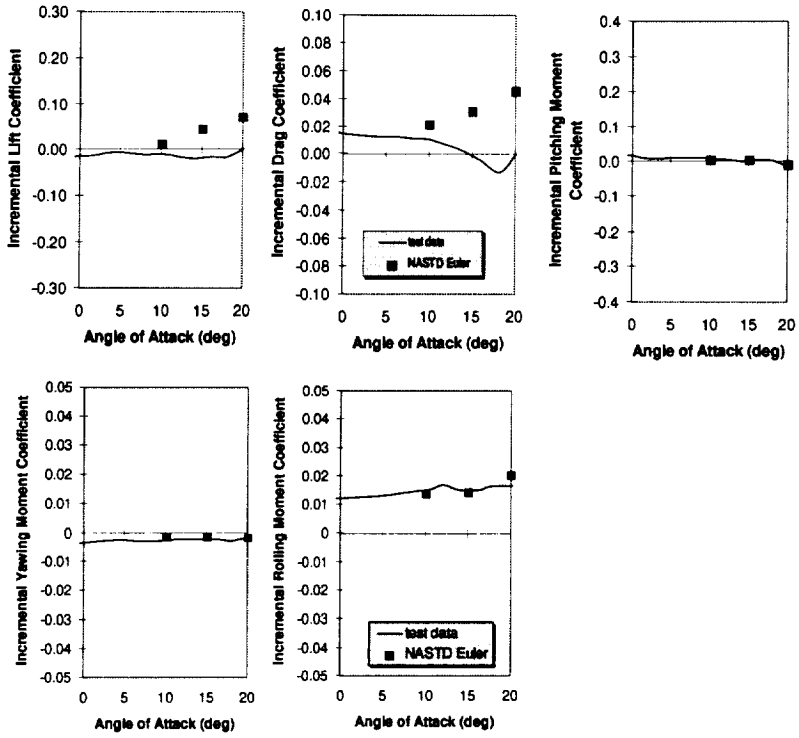

Figure 62. CFD Incremental Force and Moment Comparisons With Test Data, ACWFT With Asymmetric Elevon Deflection, Mach 0.6.

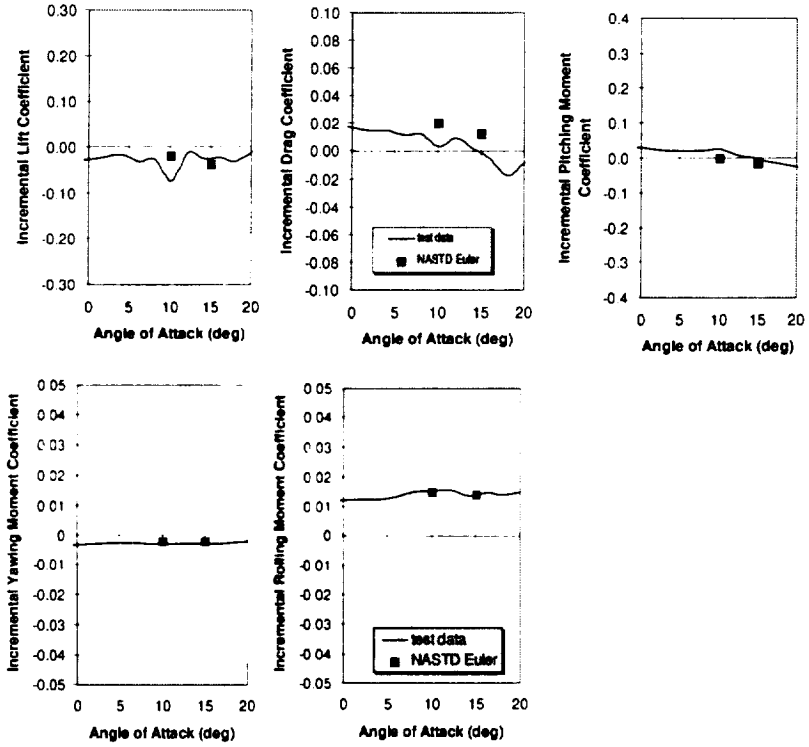

Figure 63. CFD Incremental Force and Moment Comparisons With Test Data, ACWFT With Asymmetric Elevon Deflection, Mach 0.9.

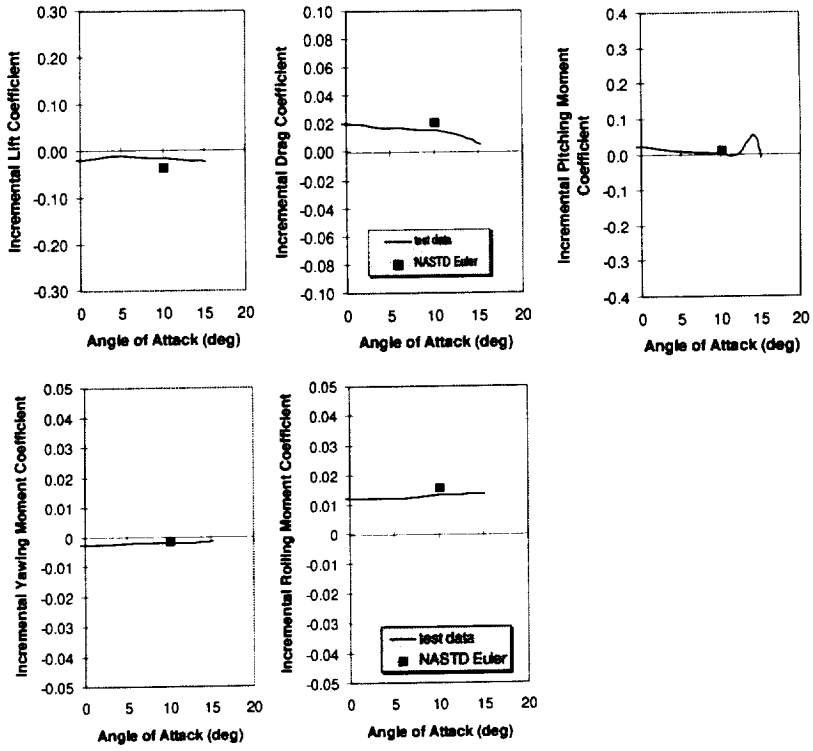

Figure 64. CFD Incremental Force and Moment Comparisons With Test Data, ACWFT With Asymmetric Elevon Deflection, Mach 1.2.

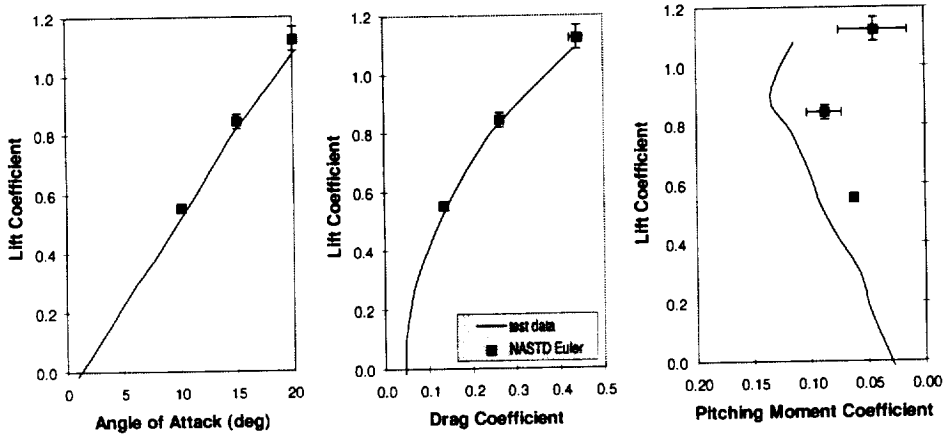

Figure 65. CFD Force and Moment Comparisons With Test Data, ACWFT With Deflected Body Flap, Mach 0.6.

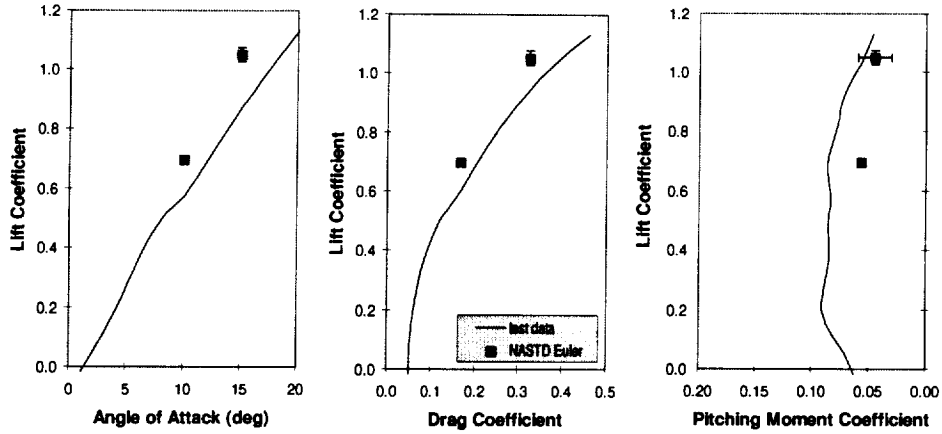

Figure 66. CFD Force and Moment Comparisons With Test Data, ACWFT With Deflected Body Flap, Mach 0.9.

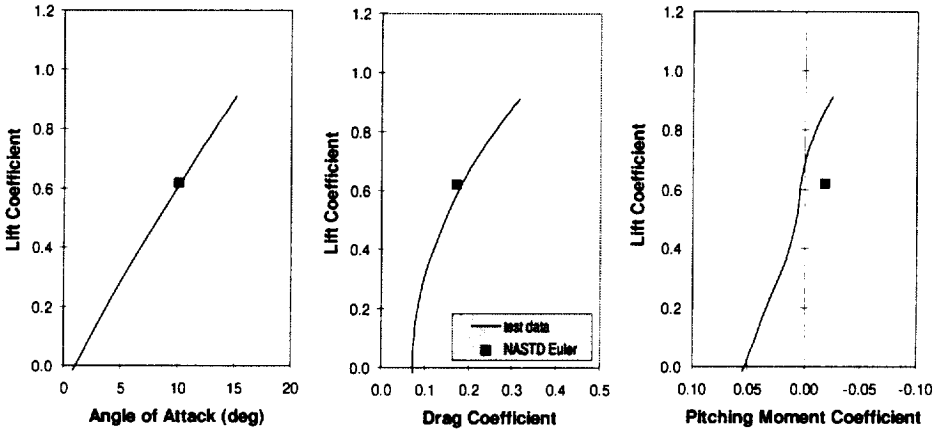

Figure 67. CFD Force and Moment Comparisons With Test Data, ACWFT With Deflected Body Flap, Mach 1.2.

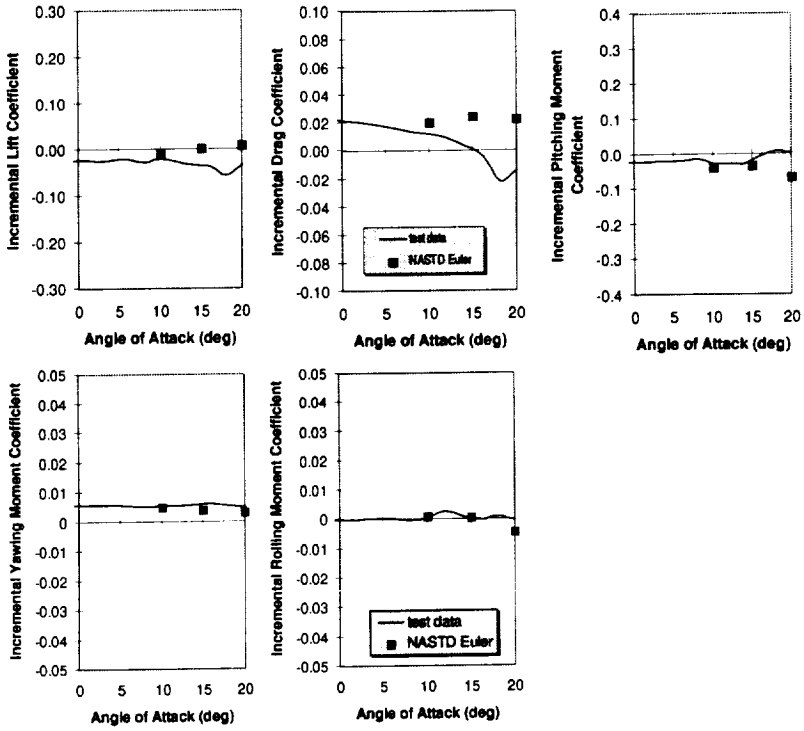

Figure 68. CFD Incremental Force and Moment Comparisons With Test Data, ACWFT With Deflected Body Flap, Mach 0.6.

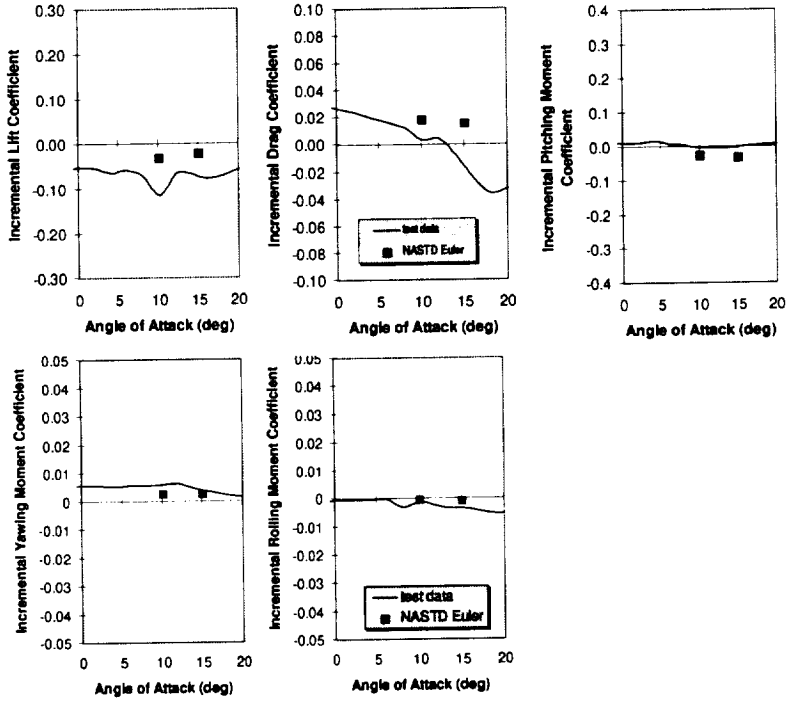

Figure 69. CFD Incremental Force and Moment Comparisons With Test Data, ACWFT With Deflected Body Flap, Mach 0.9.

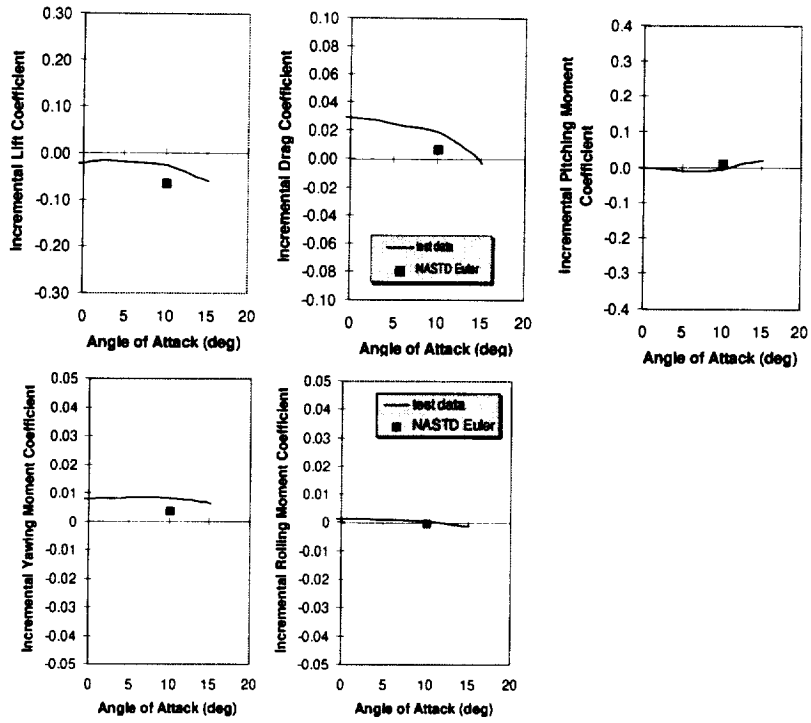

Figure 70. CFD Incremental Force and Moment Comparisons With Test Data, ACWFT With Deflected Body Flap, Mach 1.2.

REPORT DOCUMENTATION PAGE

Form Approved
OMB No. 0704-0188

1. AGENCY USE ONLY *(Leave blank)*	2. REPORT DATE	3. REPORT TYPE AND DATES COVERED
	March 1998	Contractor Report

4. TITLE AND SUBTITLE
Euler Technology Assessment for Preliminary Aircraft Design - Unstructured/Structured Grid NASTD Application for Aerodynamic Analysis of an Advanced Fighter/Tailless Configuration

5. FUNDING NUMBERS
NAS1-20342, Task 13
WU 522-22-11-01

6. AUTHOR(S)
Todd R. Michal

7. PERFORMING ORGANIZATION NAME(S) AND ADDRESS(ES)
Boeing Company
St. Louis, Missouri

8. PERFORMING ORGANIZATION REPORT NUMBER

9. SPONSORING/MONITORING AGENCY NAME(S) AND ADDRESS(ES)
National Aeronautics and Space Administration
Langley Research Center
Hampton, VA 23681-0001

10. SPONSORING/MONITORING AGENCY REPORT NUMBER
NASA/CR-1998-206947

11. SUPPLEMENTARY NOTES
Langley Technical Monitor: Farhad Ghaffari

12a. DISTRIBUTION/AVAILABILITY STATEMENT
Unclassified-Unlimited
Subject Category 02
Distribution: Standard
Availability: NASA CASI (301) 621-0390

12b. DISTRIBUTION CODE

13. ABSTRACT *(Maximum 200 words)*

This study supports the NASA Langley sponsored project aimed at determining the viability of using Euler technology for preliminary design use. The primary objective of this study was to assess the accuracy and efficiency of the Boeing, St. Louis unstructured grid flow field analysis system, consisting of the MACGS grid generation and NASTD flow solver codes. Euler solutions about the Aero Configuration/Weapons Fighter Technology (ACWFT) 1204 aircraft configuration were generated. Several variations of the geometry were investigated including a standard wing, cambered wing, deflected elevon, and deflected body flap. A wide range of flow conditions, most of which were in the non-linear regimes of the flight envelope, including variations in speed (subsonic, transonic, supersonic), angles of attack, and sideslip were investigated. Several flowfield non-linearities were present in these solutions including shock waves, vortical flows and the resulting interactions. The accuracy of this method was evaluated by comparing solutions with test data and Navier-Stokes solutions. The ability to accurately predict lateral-directional characteristics and control effectiveness was investigated by computing solutions with sideslip, and with deflected control surfaces. Problem set up times and computational resource requirements were documented and used to evaluate the efficiency of this approach for use in the fast paced preliminary design environment.

14. SUBJECT TERMS
Computational Fluid Dynamics, Euler Formulation, Preliminary Aircraft Design, Advanced Fighter Design, Vortical Flows, Unstructured/Structured Grid NASTD

15. NUMBER OF PAGES
55

16. PRICE CODE
A04

17. SECURITY CLASSIFICATION OF REPORT	18. SECURITY CLASSIFICATION OF THIS PAGE	19. SECURITY CLASSIFICATION OF ABSTRACT	20. LIMITATION OF ABSTRACT
Unclassified	Unclassified	Unclassified	